國立臺灣大學理學院物理學研究所

碩士論文

Department of Physics

College of Science

National Taiwan University

Master's Thesis

COSMOS 場域的後星爆星系：機械學習辨識以及快速淬滅路徑的演化分析

Post-starburst Galaxies in the COSMOS Field: Machine Learning Identification and Evolutionary Insights into the Rapid Quenching Path

范凱翔

Kai-Xiang Fan

指導教授: 吳柏鋒 博士

Advisor: Po-Feng Wu Ph.D.

中華民國 113 年 7 月

July, 2024

doi:10.6342/NTU202401965

國立臺灣大學碩士學位論文
口試委員會審定書
MASTER'S THESIS ACCEPTANCE CERTIFICATE
NATIONAL TAIWAN UNIVERSITY

（論文中文題目）(Chinese title of Master's thesis) 請刪除本行自行填寫

（論文英文題目）(English title of Master's thesis) Post-starburst Galaxies in the COSMOS Field: Machine Learning Identification and Evolutionary Insights into the Fast Quenching Path

本論文係__范凱翔__(姓名)_R11222049_（學號）在國立臺灣大學_物理系物理所_(系/所/學位學程)完成之碩士學位論文，於民國_113_年_7_月_10_日承下列考試委員審查通過及口試及格，特此證明。

The undersigned, appointed by the Department / Institute of _____Physics_____ on __10__(date)__7___ (month)__2024___ (year) have examined a Master's thesis entitled above presented by__Kai-Xiang Fan__ (name)___R11222049___ (student ID) candidate and hereby certify that it is worthy of acceptance.

口試委員 Oral examination committee:

吳相鋒	王為豪	
（指導教授Advisor）		

doi:10.6342/NTU202401965

doi:10.6342/NTU202401965

Acknowledgements

I would like to express my sincere gratitude to everyone who has contributed to the completion of this thesis.

First and foremost, I am deeply thankful to my advisor, Professor Po-Feng Wu, for his unwavering support, invaluable guidance, and scholarly insights throughout the entire research process. His mentorship has been instrumental in shaping the direction of this work.

I extend my appreciation to the members of my thesis committee, Wei-Hao Wang, and Yen-Ting Lin, for their constructive feedback and expertise, which enriched the quality of this research.

I am grateful to my colleagues and peers who have offered their encouragement, insightful discussions, and assistance throughout the various stages of this project. Their collaborative spirit has been a source of inspiration.

Last but not least, I want to express my deepest appreciation to my family and friends for their unwavering encouragement and understanding during this challenging academic journey.

This work would not have been possible without the collective support and encourage-

doi:10.6342/NTU202401965

ment of all those mentioned above. Thank you for being an integral part of this academic endeavor.

doi:10.6342/NTU202401965

中文摘要

後星暴星係是最近在其恆星形成過程中經歷了顯著截斷的天體。研究這些過渡物體可以為星系演化提供有價值的見解。正在進行和即將進行的調查提供了覆蓋廣闊天空區域的大量光度數據。對這些數據應用光譜能量分佈（SED）擬合技術將識別出大量的星暴後星系，但計算時間較長。機器學習 (ML) 技術可以提供更快、更有效率的替代方案。

我使用了 COSMOS2020 目錄，它收集了 1.27 $\deg^2$ 宇宙演化巡天 (COSMOS) 場的測量結果。本研究追求兩個目標：(1) 建構獨立於 SED 擬合的 ML 分類模型來辨識星暴後星系。(2) 研究具有廣泛紅移和質量的後星暴星系，以研究透過星系質量函數的快速猝滅。

ML 方法可以利用光學 + 近紅外線資訊很好地辨識後星暴星系。使用 XGBoost 分類器，模型可以在犧牲召回率（0.1）的同時實現高精度（0.85）。透過未來的光學/近紅外線巡天，該模型可以有效地識別大量後星暴星系。

本研究提出了質量為 $log(M_*/M_\odot) > 8$、$0.1 < z < 3.0$ 的恆星形成、靜止和後星暴星系的質量函數。透過研究後星暴星系質量函數的轉變並將其與靜止星系的質量函數進行比較，可以限制它們的壽命。靜止星系質量函數的累積可以透過後星暴星系的轉變來解釋。在 $log(M_*/M_\odot) > 10$ 的高品質下，星暴後星系的壽命估計為 60-300 Myr。然而，在低質量 $log(M_*/M_\odot) < 10$ 時，在 $z < 1$ 處進行了更長的

doi:10.6342/NTU202401965

星暴後壽命估計 > 1 Gyr。後星暴星系轉變為靜止狀態的回收情景可以解決這個問題，顯示只有不到 60% 的後星暴星系直接轉變為靜止狀態。然而，還需要進一步的測試來證實這項結果。

關鍵字：天文數據分析、機械學習、星系、星系演化、恆星質量函數

doi:10.6342/NTU202401965

Abstract

Post-starburst galaxies are objects that have recently experienced a significant truncation in their star formation. Studying these transitional objects can offer valuable insights into galaxy evolution. Ongoing and forthcoming surveys provide vast photometric data covering extensive sky areas. Applying spectral energy distribution (SED) fitting techniques to these data will identify a large number of post-starburst galaxies, but the computation time is lengthy. Machine learning (ML) techniques can provide faster and more efficient alternatives.

I used the COSMOS2020 catalog, which gathers measurements in the 1.27 deg^2 Cosmic Evolution Survey (COSMOS) field. This research pursues two objectives: (1) Construct a SED-fitting-independent ML classification model to identify post-starburst galaxies. (2) Studying post-starburst galaxies across a wide range of redshifts and masses to investigate rapid quenching through galaxy mass function.

The ML methods can identify post-starburst galaxies well with the optical+NIR infor-

doi:10.6342/NTU202401965

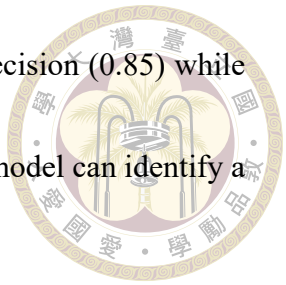

mation. With the XGBoost classifier, the model can achieve high precision (0.85) while sacrificing the recall rate (0.1). With future optical/NIR surveys, the model can identify a large number of post-starburst galaxies efficiently.

The mass functions of star-forming, quiescent, and post-starburst galaxies with masses $log(M_*/M_\odot) > 8$ at $0.1 < z < 3.0$ are presented in this study. By studying the transition of the mass functions of post-starburst galaxies and comparing them with those of quiescent galaxies, their lifetimes can be constrained. The buildup of the mass functions of quiescent galaxies can be explained by the transition of post-starburst galaxies. At high masses with $log(M_*/M_\odot) > 10$, the lifetime of post-starburst galaxies is estimated to be 60-300 Myr. However, a longer post-starburst lifetime estimate > 1 Gyr is carried out at $z < 1$ at low masses $log(M_*/M_\odot) < 10$. A recycling scenario for post-starburst galaxies transitioning into quiescence can address this issue, indicating that less than 60% of post-starburst galaxies transition directly into quiescence. However, further testing is required to confirm this result.

Keywords: Astronomy data analysis, Machine learning, Galaxies, Galaxy evolution, Stellar mass functions

doi:10.6342/NTU202401965

Contents

doi:10.6342/NTU202401965

doi:10.6342/NTU202401965

List of Figures

doi:10.6342/NTU202401965

doi:10.6342/NTU202401965

List of Tables

doi:10.6342/NTU202401965

doi:10.6342/NTU202401965

Denotation

AUROC	Area under the receiver operating characteristic curve
IR	Infrared
ML	Machine learning
NIR	Near-infrared
UV	Ultraviolet
NUV	Near-ultraviolet
FUV	Far-ultraviolet
PSBs	Post-starburst galaxies
SEDs	Spectral energy distributions

doi:10.6342/NTU202401965

doi:10.6342/NTU202401965

Chapter 1 Introduction

In the universe, the galaxy population exhibits bimodal properties in both color and structure. Most of them can be categorized as either the red sequence, characterized by those with quiescent star formation, old stellar populations, and an elliptical structure, or the blue cloud, with active star formation and a spiral structure. Over the past two decades, Observations indicate an increase in the quiescent population in both number density and mass function as redshift decreases (Davidzon et al. 2017; Ilbert et al. 2013; Muzzin et al. 2013; Weaver et al. 2023b). Since quiescent galaxies cannot form new stars, their growth suggests the transition from star-forming to quiescent, known as galaxy "quenching." The quenching processes involve galaxies changing their structure and stellar population, as well as various feedback mechanisms. Understanding the mechanisms of quenching is now one of the most central questions in the field of galaxy evolution.

Several empirical studies have attempted to uncover evolutionary mechanisms. Kauffmann et al. (2003) showed clear differences in the stellar mass distributions between the two populations, with low-mass galaxies dominating the star-forming population and high-mass galaxies dominating the quiescent population. They noted a sharp transition in galaxy properties occurring at a stellar mass of $\sim 10^{10.5}\,M_{\odot}$. Afterward, Peng et al. (2010) proposed that the quenching process may be predominantly driven by two modes: mass

doi:10.6342/NTU202401965

quenching and environmental quenching, with an approximate threshold of $\sim 10^{10.5}\ M_{\odot}$ demarcating these modes. Mass quenching occurs when galaxies grow so massive that mechanisms such as active galactic nuclei (AGN) feedback or gravitational heating prevent gas from cooling and forming new stars. Environmental quenching, on the other hand, is driven by external factors. When galaxies enter dense environments like galaxy clusters, interactions such as ram pressure stripping or galaxy harassment remove or heat their gas reservoirs, inhibiting star formation. Both processes are crucial in shaping galaxy evolution. In addition to empirical studies in galaxy evolution, a more direct approach involves studying galaxies undergoing transition. One type of such galaxies is the post-starburst (PSB) galaxy (some will call them E+A or K+A galaxies). PSBs are young quiescent galaxies whose star formation has recently and rapidly ceased. One defining feature of PSBs is their strong Balmer absorptions, attributed mainly to A-type stars in their spectral energy distributions (SEDs) (Dressler & Gunn 1983). PSBs at low redshift have been associated with major mergers with evidence of tidal features or disturbed morphologies (e.g., Goto 2005; Yang et al. 2008; Zabludoff et al. 1996). Simulations indicate that these spectral features suggest a recent, brief, and intense period of star formation, followed by rapid truncation. The lifetime (τ) of PSBs is generally shorter. Simulations estimate it to be between 100 and 600 Myr (Snyder et al. 2011; Wild et al. 2009), and observations using spectral template fitting methods suggest a few Myr to around 1 Gyr (e.g., Ciesla et al. 2016; Quintero et al. 2004), indicating a rapid transition to quiescence. Due to short living time, they are rare at $z < 2$ with fractions varying from 0.1% to 1% (Wild et al. 2016).

Numerous techniques have been developed to identify galaxies in this phase. Among the earlier searches for PSBs, spectroscopic surveys of clusters focused on galaxies with

doi:10.6342/NTU202401965

strong Balmer absorption lines, characteristic of starburst galaxies, but with no or weak emission lines, indicating no/weak ongoing star formation (Couch & Sharples 1987; Dressler et al. 1999). PSB selections typically rely on strong Balmer absorption features to identify recent star formation, while also requiring low nebular emission line flux to exclude ongoing star formation. In terms of broad-band data based on large sky surveys, various photometric methods are also used for PSBs. The rest frame UVJ diagram is often used to select high-redshift quiescent galaxies, with PSBs located in a unique position representing the younger quiescent population in this space (e.g., Belli et al. 2019; Whitaker et al. 2012; Wu et al. 2020). The principal-components-analysis (PCA) selection (Wild et al. 2007) and the super color method (Wild et al. 2014) have been widely used to select higher redshift PSB samples as well. Recently, machine learning (ML) methods can be used on spectroscopic samples to identify potential PSBs using ultraviolet (UV) to infrared (IR) photometric data from large sky surveys (French & Zabludoff 2018).

In recent years, large sky surveys have led us to a new era of data-driven astronomy. The Euclid Wide Survey[1] (EWS) (Euclid Collaboration et al. 2022b) will cover a total area of $\sim 15,000\mathrm{deg}^2$ with optical I and near-infrared (NIR) YJH broadband measurements. Meanwhile the Legacy Survey of Space and Time [2] (LSST) led by the Rubin Observatory (USA, Ivezić et al. 2019) is approaching, aiming to explore more than $18,000\mathrm{deg}^2$ with UV u and optical $grizy$ broadband in 10-year operation. The Rubin Observatory LSST and Euclid EWS combined area is expected to cover approximately 8,000 deg^2 (Euclid Collaboration et al. 2022b), which will include optical and NIR information on over 500 million galaxies. SED fitting to these data will identify a huge number of PSBs. By analyzing these data, researchers will be able to gather a much larger sample of post-starburst

[1] https://www.esa.int/Science_Exploration/Space_Science/Euclid
[2] https://www.lsst.org/

doi:10.6342/NTU202401965

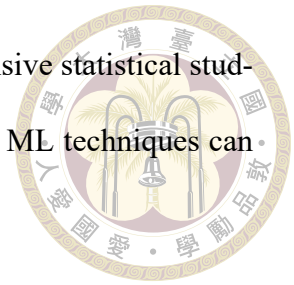

galaxies than ever before, enabling them to conduct more comprehensive statistical studies. However, the computation of SED fitting will take a long time. ML techniques can provide faster and more efficient alternatives.

To achieve this, I used the most recent COSMOS catalog COSMOS2020 (Weaver et al. 2022) for my research. This catalog includes measurements spanning a broad range of wavelengths, from UV to IR, which is the same range that most current and future surveys cover. All of the measurements in this catalog are within the Cosmic Evolution Survey (COSMOS) field, a substantial area of 2deg^2 used for studies focused on galaxy evolution. This wide wavelength coverage enables us to determine which broadband measurements are crucial for machine learning. Initially, this research pursues two objectives: (1) Develop a machine learning classification model that can independently identify PSBs in upcoming and ongoing surveys, without relying on spectral energy distribution (SED) fitting. (2) Use this model on current large survey data to create an extensive sample of PSBs and conduct statistics across a wider mass range than in previous studies. Unfortunately, my study cannot make a highly complete model. So I conduct two works for PSBs: (1) building an ML classification model and (2) conducting evolution analyses in the COSMOS2020 catalog. The second work may serve as a reference for future statistical analysis when implementing the model, especially the low-mass PSB behavior.

This thesis is organized as follows. Chapter 2 begins by introducing the catalog and data processing related to COSMOS2020. In Chapter 3, the results of machine learning and the evolution of galaxies in number density and mass function are presented. These results are then interpreted in Chapter 4. Finally, Chapter 5 concludes with a summary and offers perspectives for future PSB studies. The results presented here adopt a standard ΛCDM cosmology with $H_0 = 70\,km\,s^{-1}\,Mpc^{-1}$, $\Omega_{m,0} = 0.3$, and $\Omega_{\Lambda,0} = 0.7$, and all magnitudes

doi:10.6342/NTU202401965

and colors are in the AB system (Oke & Gunn 1983).

doi:10.6342/NTU202401965

doi:10.6342/NTU202401965

Chapter 2 Data

The COSMOS2020 catalog (Weaver et al. 2022) is used for ML and galaxy evolution analyses. Sample selection functions of the two works, ML and galaxy evolution, lead to two samples: the IR-selected sample and the learning sample, which are described in the following section.

2.1 COSMOS2020

COSMOS2020 is the latest UV-optical-IR COSMOS photometric redshift catalog. It consists of $\sim$ $1,000,000$ galaxies identified from a NIR *izYJHK*$_s$ `CHI-MEAN` co-added image (Bertin 2010; Szalay et al. 1999). Covering a $\sim$2 deg^2 area, the catalog includes many broad and narrow band observations spanning wavelengths from ultraviolet to NIR, including *u*-band measurements from the Canada-France-Hawaii Telescope (CFHT) via the CFHT Large Area U-band Deep Survey (Sawicki et al. 2019), optical from the second public data release (PDR2) of the Hyper Suprime-Cam Subaru Strategic Program (HSC-SSP) *grizy* broadband data (Aihara et al. 2019) and Subaru Suprime-Cam (SC) $Bg^+Vr^+i^+z^+z^{++}$ broadband data (Taniguchi et al. 2015, 2007), NIR from the UltraVISTA survey fourth data release (DR4) *YJHK*$_s$ broadband data and *NB118* narrowband data (McCracken et al. 2012; Moneti et al. 2023), and all *Spitzer*/IRAC IR data in all four channels from the Cosmic Dawn Survey (Euclid Collaboration et al. 2022a). Further-

doi:10.6342/NTU202401965

more, the COSMOS2020 catalog includes some basic measurements, such as the near-UV (*NUV*) and far-UV (*FUV*) from the COSMOS GALEX catalog (Zamojski et al. 2007), and X-ray from the Chandra COSMOS Legacy survey (Civano et al. 2016; Marchesi et al. 2016). Intermediate and narrow bands from Subaru/Suprime-Cam (Taniguchi et al. 2015, 2007) and VISTA (Milvang-Jensen et al. 2013) are provided for precise photometric redshift determinations, consistent with the previous COSMOS catalog (Laigle et al. 2016).

In COSMOS2020, two different techniques are applied for photometry extraction, resulting in two independent sub-catalogs. The first catalog, called CLASSIC, is created through aperture method with `Source Extractor` (Bertin & Arnouts 1996) for optical/NIR and with `IRACLEAN` (Hsieh et al. 2012) for IR. The second catalog, named THE FARMER, is constructed through the profile-fitting technique with `THE FARMER` (Weaver et al. 2023a), which uses `The Tractor` (Lang et al. 2016) to construct and implement parametric modeling to estimate source fluxes. Physical properties of galaxies, such as photometric redshifts (hereafter called photo-z), rest-frame fluxes/magnitudes, and stellar masses (M), are measured by fitting their SEDs for each photometric catalog through `LePhare` (Arnouts et al. 2002; Ilbert et al. 2006) and `EAzY` (Brammer et al. 2008). This results in each source being associated with four sets of measurements. My work adopts THE FARMER catalog with physical measurements performed by `LePhare` using several galaxy spectral templates from Polletta et al. (2007) and Bruzual & Charlot (2003). Rest-frame absolute magnitudes are derived from best-fit spectral templates using an interpolation method. Stellar masses were estimated using the tau+delayed models of Bruzual & Charlot (2003), assuming an initial mass function (IMF) based on Chabrier (2003). In summary, by employing extensive deep imaging, distinct photometric techniques, and independent SED fitting, COSMOS2020 can offer us a more accurate understanding of

doi:10.6342/NTU202401965

galaxy populations. For further information, such as photometric uncertainties and photo-z accuracy, see Weaver et al. (2022) for details.

2.2 Sample selection

I used The Farmer catalog in conjunction with photo-z, rest-frame magnitudes, and stellar mass M estimates provided by `LePhare`. This combination is the basis for our ML models and galaxy evolution analyses. It enables direct comparisons with similar literature (e.g., Davidzon et al. 2017; Ilbert et al. 2013; Weaver et al. 2023b), particularly for evolution work. Throughout this study, this combination is referred to as COSMOS2020, unless otherwise noted.

The selection of galaxies for this study, both in ML and galaxy evolution work, adheres to specific criteria, referred to Weaver et al. (2023b). Initially, galaxies[3] are chosen to be free from contamination by bright stars in the combined region of HSC, Suprime-Cam, and UltraVISTA. Although the COSMOS survey covers a total area of 2 deg^2, I focus on a data-concentrated region of 1.279 deg^2 (Weaver et al. 2022). This area corresponds to the overlap of the deep NIR UltraVISTA, optical HSC, and Subaru Suprime-Cam images, excluding the halos of bright stars that could introduce contamination.

As mentioned in Sect. 2.1, `LePhare` uses an interpolation method to derive the absolute magnitudes. This may cause significant uncertainties in their rest-frame colors when classifying galaxies in the $NUVrJ$ space, particularly at redshifts higher than 2.6, where absolute magnitudes are calculated by an extrapolation method. For example, at $z = 2.6$, M_J corresponds to redder observed wavelengths than those in IRAC Ch2, the reddest band used for SED fitting in `LePhare`. To avoid this issue, our study only focuses on galaxies

[3]Galaxies are selected by `lp_type` = 0, see catalog documentation.

doi:10.6342/NTU202401965

within the redshift range of $z < 3.0$ to ensure a precise classification. Photo-z estimates are taken from `lp_zPDF`, representing the median of the redshift likelihood distribution. M estimates are obtained from `lp_mass_med`, signifying the median of the mass likelihood distributions.

For evolution analyses, the initial sample of 861,048 galaxies is selected with a successful photometry extraction in `THE FARMER` modeling process[4]. The selection is further confined to the range of $0.1 < z < 3.0$ in the contiguous 1.27 deg^2 `COMBINED` region[5], finding 566,893 galaxies. Subsequently, sources with non-null M, rest-frame magnitudes m_{NUV}, m_r, m_J, and valid[6] m_{ch1} are chosen for subsequent galaxy classification and mass-completeness steps in Section 2.3 and Section 2.4.

To achieve a precise classification and a reliable mass function, it is imperative to have accurate redshift measurements and precise measurements of stellar masses. To simplify the process, sources with redshifts that have a 68% confidence range outside the $z \pm 0.5$ are removed, resulting in 455,263 sources. Furthermore, sources with an unreliable SED fit with reduced $\chi^2 > 10$ are also excluded. These two cuts create a sample of 453,795 galaxies, the starting point for further analysis.

Achieving accurate measurements of stellar masses at redshifts $z \gtrsim 2 - 3$ requires IR detection as it contains more information on stellar populations, especially for older ones. To ensure mass completeness, sources with $m_{ch1} > 26$ AB ($S/N \lesssim 5$) are excluded. This eliminates about 50% of the sources that fall below the mass-completeness limit detailed in Section 2.4. The final sample, referred to as the IR-selected sample, consists of 264,493 galaxies.

[4] `MODEL_FLAG` = 0
[5] `FLAG_COMBINED` = 0
[6] `###_VALID`, set to True where FLUX or FLUXERR is trustworthy. `###` is the name of filter.

doi:10.6342/NTU202401965

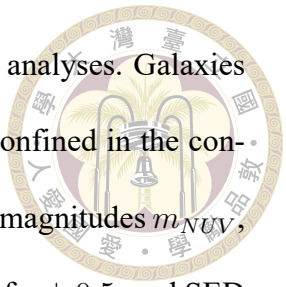

For ML, the selection functions are similar to those of the evolution analyses. Galaxies are selected with successful photometry extraction and then further confined in the contiguous 1.27 deg^2 `COMBINED` region. Sources with non-null rest-frame magnitudes m_{NUV}, m_r, m_J, redshift at $0 < z < 3$ with 68% confidence inside the range of $z \pm 0.5$, and SED fit more than 8 filters[7] are selected. The final learning dataset, referred to as the learning sample, was selected from those with valid fluxes and $S/N \gtrsim 5$ in the *u, g, r, i, z, Y, J, H,* K_s bands. The learning sample includes 291,511 galaxies, and 3015 of them are PSBs. PSB labels are defined as eq 2 in Section 2.3.

In general, these processes ensure the sample is accurate and complete for each galactic type, leading to robust results.

2.3 Galaxy classification

Several studies have proposed different techniques to classify galaxies using broadband photometry. One of the most commonly used methods is to use rest-frame color-color diagrams, which are quick and easy to use with large photometric datasets. These diagrams are handy for quiescent populations, making it easier to distinguish them from dusty star-forming galaxies. The two most widely used techniques are rest-frame *UVJ* (e.g. Muzzin et al. 2013; Williams et al. 2009) and *NUVrJ* or *NUVrK* (e.g. Arnouts et al. 2013; Ilbert et al. 2013; Noirot et al. 2022; Weaver et al. 2023b). The *U-V* or *NUV-r* color is sensitive to recent star formation activity, effectively distinguishing between star-forming and quiescent galaxies. In contrast, the *V-J* or *r-J* color serves as an indicator of the overall stellar population age and dust content, differentiating red dusty star-forming galaxies from quiescent galaxies.

[7] `lp_NbFilt` > 8

doi:10.6342/NTU202401965

To establish a well-defined criterion for color selection, it is crucial to define the PSBs in the color-color space. In the NUVrJ color-color space, PSBs typically occupy a specific region that reflects their recent cessation of star formation and intermediate stellar populations. They are characterized by recent star formation but no ongoing star formation, and they are less dusty than actively star-forming galaxies. Using this feature, one can coadd with the method by tracing their stellar age to define the demarcation of PSBs in color-color diagrams, e.g., *UVJ* colors (Belli et al. 2019; Whitaker et al. 2012; Wu et al. 2020).

In this study, I adopt the rest-frame *NUVrJ* colors to classify our sample into star-forming, quiescent, and PSB classes. I used the criteria from Ichikawa & Matsuoka (2017), who apply the age around 1Gyr in the single-burst/exponentially declining model to define the PSB demarcation. Figure. 1 demonstrate the galaxy classification at $0.1 < z < 3.0$ with redshift bin size = 0.5 in *NUVrJ* color-color space. The criteria for classifying galaxies into star-forming, quiescent, and PSB classes are as follows:

$$\text{Star-forming} \quad : \quad NUV - r < 2.5 \text{ or } NUV - r < 3(r - J) + 1 \tag{1}$$

$$\text{Quiescent} \quad : \quad NUV - r > 2.5 \text{ and } NUV - r > 3(r - J) + 1 \text{ and } r - J > 0.5 \tag{2}$$

$$\text{PSB} \quad : \quad NUV - r > 2.5 \text{ and } r - J < 0.5 \tag{3}$$

The separation between star-forming and quiescent galaxies (represented by the diagonal line in Figure 1) follows the same criterion that employed by Ilbert et al. (2013) and Weaver et al. (2022), which is nearly parallel to the dust reddening vector. The boundary separating star-forming galaxies from PSBs (illustrated by the horizontal line in Figure 1) corresponds to a time approximately 0.2 Gyr after starburst event, as modeled by Ichikawa & Matsuoka

doi:10.6342/NTU202401965

(2017). The PSB criterion can identify galaxies with recent truncation and ensure that the galaxies are not heavily reddened by dust. By classifying galaxies based on these criteria, I can conduct a comprehensive analysis of the number density evolution and accurately identify PSBs using ML techniques. Furthermore, I examined the impact of rest-frame color uncertainties on evolutionary work by varying the colors $NUV - r$ and $r - J$ by ± 1 (see Appendix 5). Varying the boundaries slightly does not have any significant impact on my results and conclusions.

2.4 Mass completeness and volume correction

To accurately determine the number density and mass function of galaxies, I must consider the stellar mass and volume of the sample. Ensuring completeness of data is crucial for investigating number density. The mass limit, determined by the minimum detectable mass of a galaxy based on its redshift and mass-to-light ratio (*M/L*), helps address limitations posed by observational capabilities.

As mentioned in Weaver et al. (2022), due to the *izYJHK*$_s$ selection function used in COSMOS2020, it is impossible to quantify m_{lim} in a single band. To determine m_{lim}, Weaver et al. (2022) cross-matched IRAC Ch1 sources of COSMOS2020 with the deeper CANDELS catalog in the overlap area ~ 200 arcmin^2. At Ch1 $m_{lim} = 26$ mag, about 75% of the CANDELS sources were also recovered by THE FARMER. Each of the studies used the 95th percentile of the rescaled mass distribution as the boundary, corresponding to a 70% completeness threshold for expected M_{lim}. To estimate the mass-completeness limit for the IR-selected sample, I followed the method presented in Weaver et al. (2023b). I started by excluding the 1% of sources with the worst-fit through χ^2 within each z-bin in Ch1 and then rescaled the stellar masses of the 30% faintest galaxies in Ch1, so that their

doi:10.6342/NTU202401965

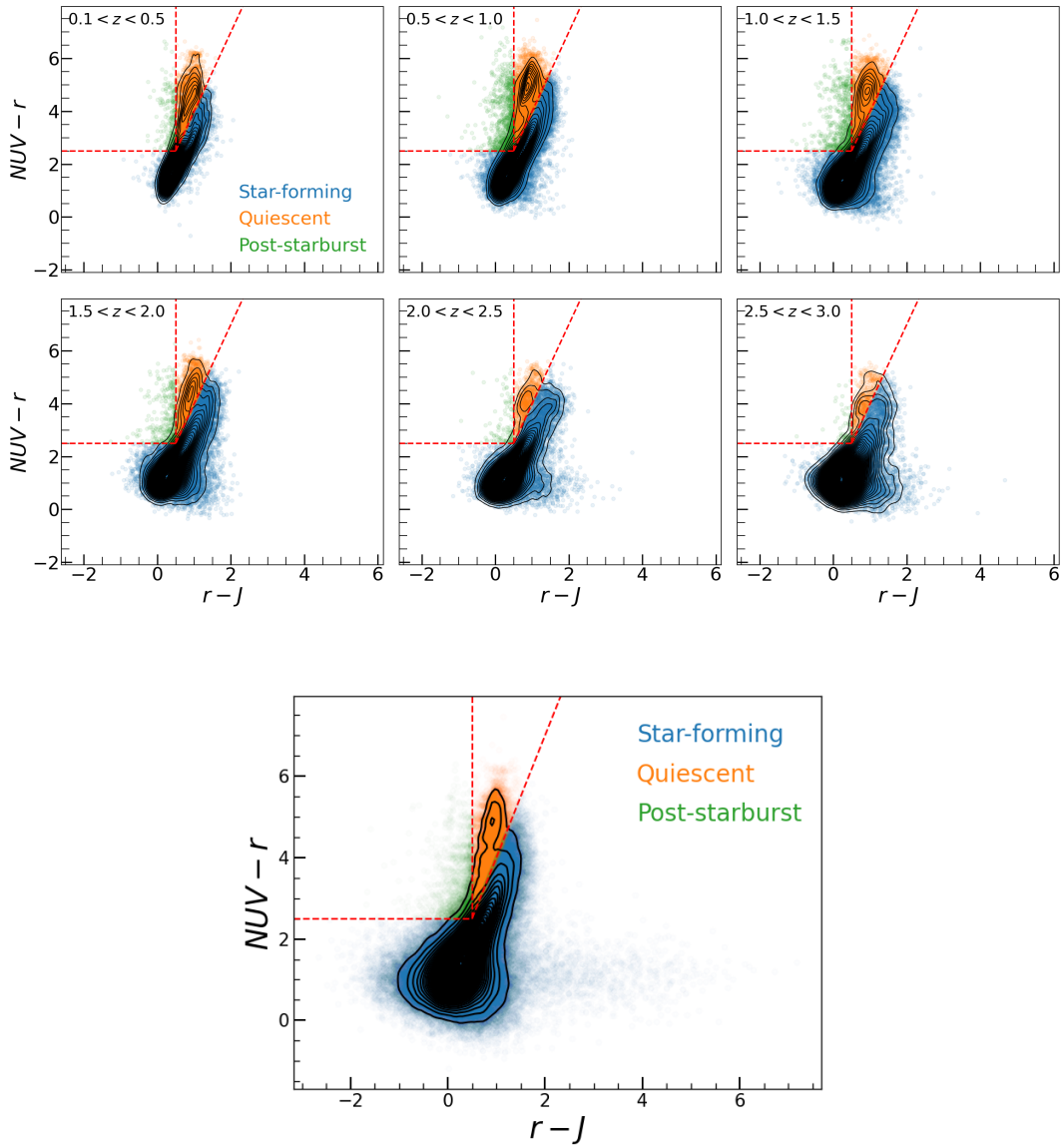

Figure 1. Top six: Identification of star-forming, quiescent, and PSBs for the IR-selected sample at redshifts of $0.1 < z < 3.0$, using a bin size of 0.5 based on their rest-frame *NUVrJ* colors. Sources above their respective mass-completeness limits are considered. Star-forming, quiescent, and PSBs are denoted by blue, orange, and green dots, respectively. The contour shows two major groups of galaxy populations in the universe. The red dashed lines represent the demarcations proposed by Ichikawa & Matsuoka (2017), defined by equations (1) to (3) for the classification of the three classes. Bottom: The same criteria applied in the top panel were used for the learning sample.

observed Ch1 apparent magnitude m_{ch1} matches the IRAC sensitivity limit $m_{lim} = 26$. I used the following equation for rescaling:

$$\log_{10}(M_{resc}) = log_{10}(M) + 0.4(m_{ch1} - 26.0) \quad (4)$$

doi:10.6342/NTU202401965

After rescaling, I calculated the limiting mass (M_{lim}) by taking the 95th percentile of the M_{resc} distribution. Finally, I fitted the log function $a \log_{10}(1+z) + b$ to each M_{lim} per z-bin for star-forming, quiescent, and PSB samples. To ensure a smoothly evolving limiting mass, I include sources with redshifts up to 5.5. Limits for ∼70% mass completeness are derived consistently for total, star-forming, quiescent, and PSB samples from $0.1 < z < 5.5$:

$$\text{Total} \quad : \quad 2.022 \times \log_{10}(1+z) + 8.025 \tag{5}$$

$$\text{Star-forming} \quad : \quad 2.014 \times \log_{10}(1+z) + 8.032 \tag{6}$$

$$\text{Quiescent} \quad : \quad 2.280 \times \log_{10}(1+z) + 8.098 \tag{7}$$

$$\text{Post-starburst} \quad : \quad 2.127 \times \log_{10}(1+z) + 7.992 \tag{8}$$

and are shown in Figure. 2.

In the bottom panel of Figure 2, it can be seen that the mass limit of the total sample is almost identical to that of the star-forming sample, regardless of the redshift. This outcome is anticipated since star-forming galaxies are the most prevalent galaxy class, significantly influencing galaxy statistics. Additionally, the higher completeness limit observed for quiescent galaxies is attributed to their dimmer nature compared to star-forming galaxies, rendering them more challenging to observe. The mass limit for PSBs falls between star-forming and quiescent galaxies.

Furthermore, accurate determination of the observable volume is indispensable in deriving the number density. I used a cosmological calculator created by Wright (2006) to determine the total survey volume in which a galaxy would be observed. To account for the impact of volume on number densities and mass functions, I used the V_{max} method,

doi:10.6342/NTU202401965

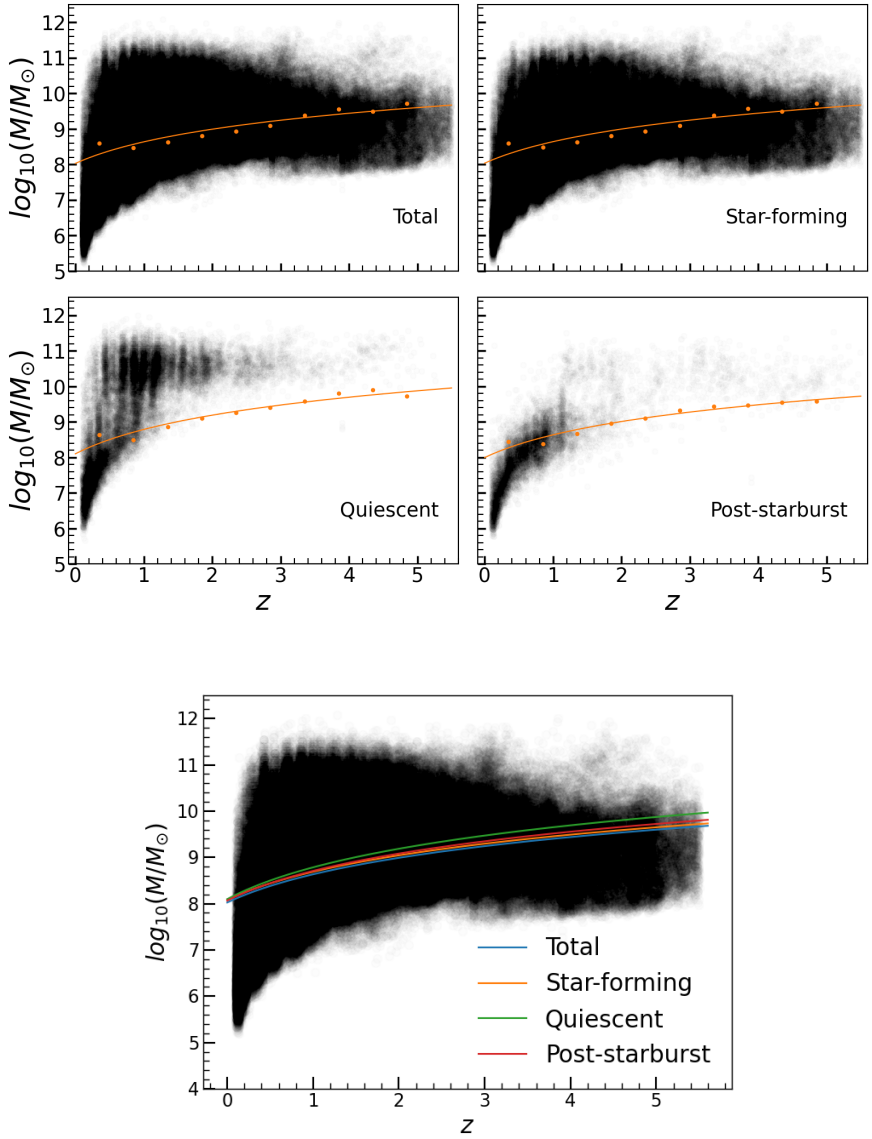

Figure 2. Top: Mass-completeness limits for the total, star-forming, quiescent, and PSB samples within $0.1 < z < 5.5$ in four panels. Here I include the higher redshift galaxies up to 5.5 to ensure a smoothly evolving limiting mass. The magnitude limits adopted from IRAC Ch1 (orange dots) to determine limits in discrete z-bins. These limits are then fitted to obtain eq(5)–eq(8). Bottom: The comparison of mass completeness limits for the total sample (blue), as well as the star-forming (orange), quiescent (green), and PSB (red) populations. The solid lines are the same as in the top panel. For clarity, the star-forming sample limit has been increased by 0.05 dex to make it visible from the star-forming one.

which assigns a weight of $1/V_{max}$ to each galaxy, where V_{max} represents the maximum observed volume of galaxies in the survey field (Schmidt 1968):

$$V_{max,i} = \frac{\Omega_{survey}}{\Omega} \times \{V_{cov}(min(z_{max,i}, z_{high})) - V_{cov}(max(z_{min,i}, z_{low}))\} \qquad (8)$$

doi:10.6342/NTU202401965

where Ω_{survey} is the solid angle subtended by the sample, $\Omega \equiv 4\pi \times \frac{180^2}{\pi^2} \cong 41253$ deg^2 is the solid angle of a sphere, and $V_{cov}(z)$ is the comoving volume at z.

doi:10.6342/NTU202401965

doi:10.6342/NTU202401965

Chapter 3 Machine Learning Identification

The ML results based on the learning sample data are presented in this chapter. This chapter discusses the broadband measurements used as input features for the ML to build the model, as well as the model limitations. In addition, it explores the factors that affect model performance and the dependence on dataset properties, such as redshift.

3.1 Feature engineering and evaluations

Supervised learning relies on input features and labels for effective model training. In this study, identifying PSBs can boil down to a binary classification problem: determining whether a given galaxy is PSB. PSB labels are assigned based on rest frame colors in the COSMOS2020 learning sample, as detailed in Sections 2.3. To determine the input features, I evaluated the performance of different combinations of feature sets on the test dataset to determine which feature sets are the best to use. The total feature set includes magnitudes and magnitude errors from the $ugrizYJHK_s$ bands and sequential colors ranging from $u-g$ to $H-K_s$. Ultimately, observed colors were selected as inputs for their superior performance and simplification to the model over other combinations (see Section 3.3).

doi:10.6342/NTU202401965

I divided the data into training, validation, and test datasets in the ratio of $9:6:10$ for the learning sample. Before incorporating the features into the model, I normalized all the features in the three datasets to reduce the dependence on specific features. The learning sample consists of 291,511 galaxies, of which 3,015 are PSBs, highlighting a significant imbalance between PSBs and other galaxies. To address this imbalance, I applied oversampling during the learning process but found that the training dataset without oversampling yielded better performance (see also Section 3.3).

The quality of the classification performance is assessed based on various metrics in learning problems. In binary classification, one can define true positive (TP; the number of target sources correctly classified as the target class, which, in our case, refers to PSBs), true negative (TN; the number of non-target sources correctly classified as the non-target class), false positive (FP; the number of non-target sources wrongly classified as the target class), and false negative (FN; the number of target sources wrongly classified as the non-target class). With these defined numbers in hand, I can further write down some important metrics in ML as follows.

1. Accuracy: the fraction of correctly classified sources (PSBs and non-PSBs) out of all sources examined.

$$\text{Accuracy} = \frac{\text{TP} + \text{TN}}{\text{TP} + \text{TN} + \text{FP} + \text{FN}} \tag{12}$$

2. Precision: also known as purity, is the fraction of correctly identified target sources (PSBs) among all sources classified as targets.

$$\text{Precision} = \frac{\text{TP}}{\text{TP} + \text{FP}} \tag{13}$$

doi:10.6342/NTU202401965

3. Recall: also known as completeness, true positive rate, or sensitivity, is the fraction of correctly identified target sources (PSBs) among all actual target sources.

$$\text{Recall} = \frac{\text{TP}}{\text{TP} + \text{FN}} \tag{14}$$

4. F1 score: the harmonic mean of precision and recall.

$$\text{F1 score} = 2 \times \frac{\text{Precision} \times \text{Recall}}{\text{Precision} + \text{Recall}} \tag{15}$$

5. Area under the receiver operating characteristic curve (AUROC): the area under the receiver operating characteristic (ROC) curve (TP versus FP).

A good classification will exhibit high precision and recall, resulting in a high F1 score and AUROC, while the definition may vary depending on different purposes.

3.2 Algorithm

I used the Python package `XGboost`[8] to identify PSBs. `XGboost`, or eXtreme Gradient Boosting, is a powerful open-source library widely used in supervised learning tasks. Known for its speed, performance, and adaptability, `XGboost` implements gradient boosting, an ensemble learning technique that combines multiple weak learners to create robust predictive models. It offers various features, including regularization techniques, customizable objective functions, and advanced tree-pruning algorithms to improve efficiency and reduce overfitting. The configuration of the model is as follows.

params = { 'max_depth': 6, 'eta': 0.01, 'objective': 'multi:softprob', 'num_class': 2,

[8] https://xgboost.readthedocs.io/

doi:10.6342/NTU202401965

’tree_method’: ’hist’, ’eval_metric’: ’mlogloss’, ’subsample’: 0.8, ’device’: ’cuda’, }

This configuration defines a gradient boosting model with the default setting ’gbtree’ booster for binary-class classification tasks. With a learning rate (eta) of 0.01, it controls the size of steps during training. I also used early stopping (early_stopping_rounds = 50; stop with lack of improvement after fifty rounds), number of boosts in each round (num_boost_round = 1; boosting a random forest in each round), and 5000 rounds of iteration. To avoid the overfitting problem, I added a validation step to evaluate the model performance.

3.3 Performances

The determination of input features is examined through the performances of different combinations of observed magnitudes (mag), observed magnitude errors (magerr), and sequential observed colors as inputs in the model. Here the imbalanced problem in the learning sample is also considered by applying the oversampling technique `SMOTE`.

Figure 3 and Figure 4 present the performance of different combinations of input features, with and without oversampling, evaluated through accuracy, precision, recall, F1 score, and AUROC as functions of the probability that the model classifies a galaxy as a PSB. Here, ”probability” refers to the likelihood that a given galaxy is identified as a PSB by the model. It is a measure derived from the confidence of the model in its classification, ranging from 0 to 1. Higher probabilities indicate greater confidence in the galaxy being a PSB, while lower probabilities suggest uncertainty or classification as a different type. Input sets of [mag + magerr + color], [mag + color], and color-only without oversampling perform relatively better than the others due to their relatively higher F1 score and AU-

doi:10.6342/NTU202401965

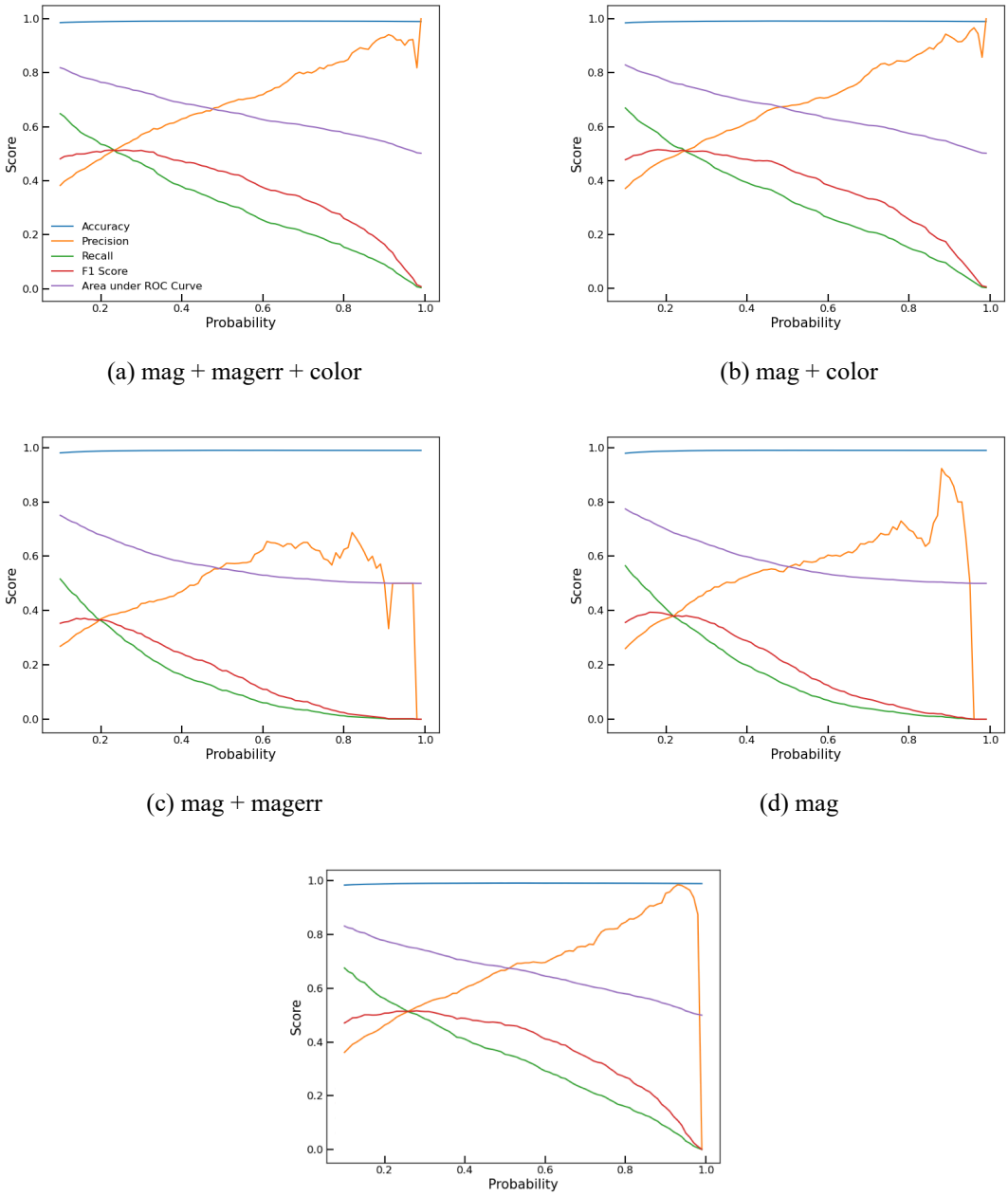

(a) mag + magerr + color

(b) mag + color

(c) mag + magerr

(d) mag

(e) color

Figure 3. The performance of different input feature combinations without oversampling is assessed using accuracy (blue), precision (orange), recall (green), F1 score (red), and AUROC score (purple) relative to the probability of being a model classified PSB. Notably, when including sequential colors, the model achieves high precision at the expense of recall, indicating its limited suitability for statistical analysis.

ROC. Different threshold decisions yield varying precision and recall. Users can adjust these thresholds based on their specific scientific objectives. Higher threshold decisions can achieve high precision in identifying PSBs, though this may result in a lower recall.

doi:10.6342/NTU202401965

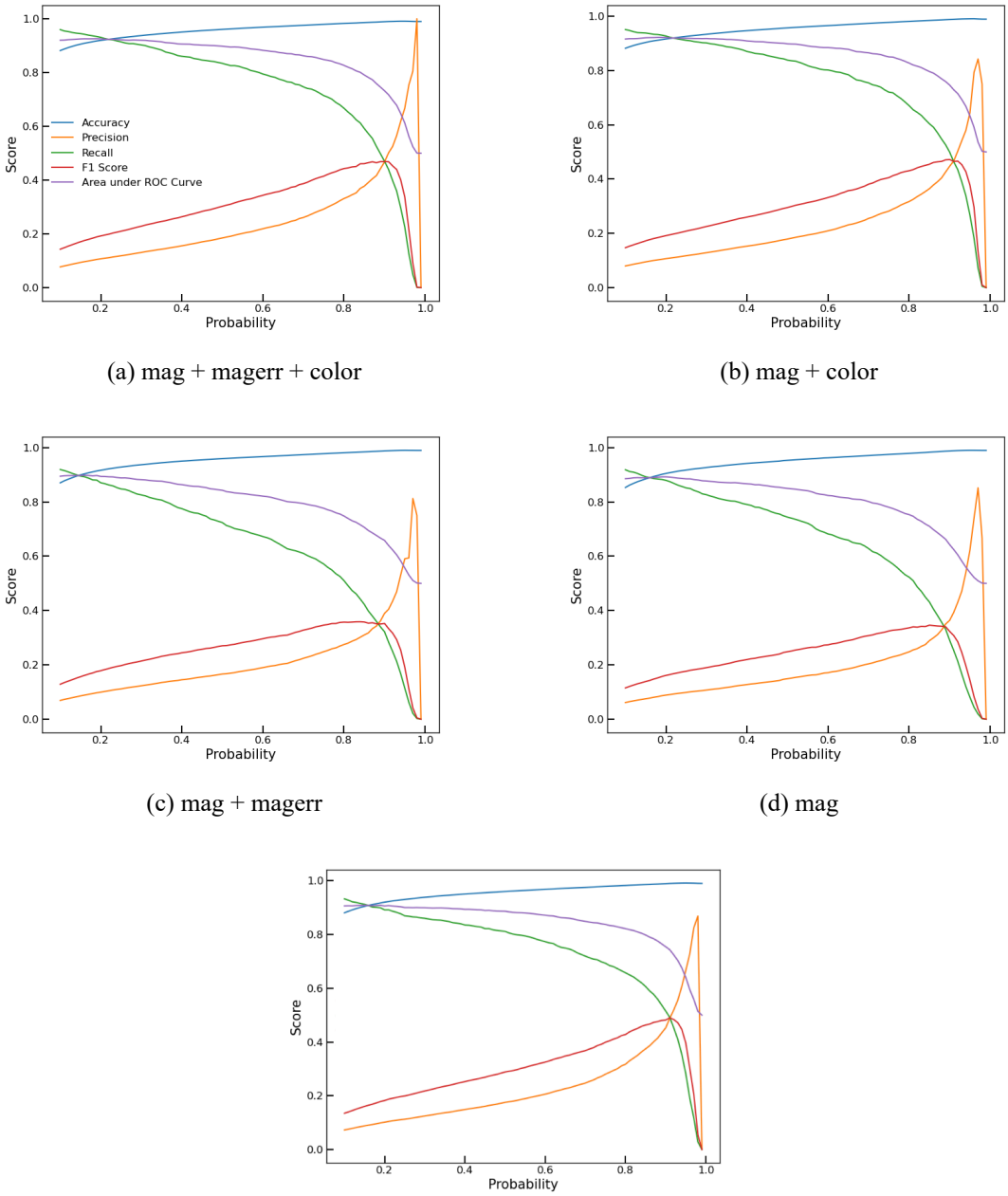

(a) mag + magerr + color

(b) mag + color

(c) mag + magerr

(d) mag

(e) color

Figure 4. The performance of different input feature combinations with oversampling is assessed using accuracy (blue), precision (orange), recall (green), F1 score (red), and AUROC score (purple) relative to the probability of being a model classified PSB. The oversampling (`SMOTE`) can enhance the recall score but resulting in lower precision and F1 score than without applying it.

The oversampling technique, shown in Figure 4, can increase recall while reducing precision, leading to lower F1 scores but higher AUROC than those without oversampling. This suggests that the model trained with oversampling can effectively capture the key features of PSBs for identification, but it also results in a higher number of false positives.

doi:10.6342/NTU202401965

This results in a high AUROC, reflecting good overall discriminatory ability, but the low F1 score highlights the trade-off between precision and recall. The issue arises because the minority class (PSBs) is oversampled to improve recall, leading to an increase in recall but a decrease in precision. Adjusting the threshold will yield results similar to those of models trained without oversampling when applying higher thresholds.

In general, the training times for different sets of inputs are less than 4 hours. Using [mag + magerr + color] takes around 4 hours, and color-only takes around 2 hours, which is about 2 times faster.

I selected the model trained with sequential I selected the model trained with sequential observed colors as inputs only, without oversampling, for the subsequent discussion and following sections to examine the prediction of PSBs. This decision was based on the model's robust performance, which compares favorably with more complex combinations and shows no significant loss in accuracy, precision, recall, or other performance metrics. Furthermore, using observed colors only simplifies the model by reducing the number of input features, which can streamline the training process and lower computational costs. The choice of the model without oversampling was deliberate because it demonstrates higher precision performance compared to the oversampled model. This ensures that PSBs identified by the model are highly reliable, even though it may lead to some sacrifice in recall.

Next, I examined the distribution of PSBs misclassified by the model based on the model without oversampling in the $NUVrJ$ diagram, I present the distribution of PSBs classified by the model at various thresholds in Figure 5. Additionally, the model performance metrics at these thresholds are displayed in Table 1, with the averages and uncertainties

doi:10.6342/NTU202401965

Table 1. Classification Performances at Different Thresholds

Threshold	Accuracy	Precision	Recall	F1 score	AUROC
0.6	0.991±0.000	0.738±0.030	0.214±0.028	0.331±0.033	0.601±0.014
0.8	0.990±0.000	0.851±0.044	0.099±0.033	0.175±0.051	0.549±0.016

The uncertainties are derived by bootstrapping.

of metrics obtained by bootstrapping. The model can well identify PSBs within the PSB region in the $NUVrJ$ diagram, with misclassified PSBs mostly located near the border. This suggests that misclassified PSBs may have spectral properties similar to those of true PSBs, which could be why they were classified as PSBs.

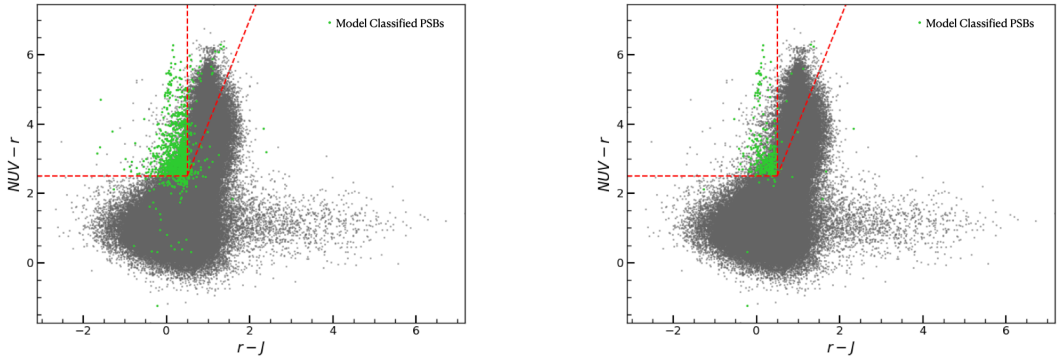

Figure 5. The model classified PSB (green dots) distribution in $NUVrJ$ diagrams. The red dash lines are demarcations of star-forming, quiescent, and PSBs. Left: Threshold = 0.6. Right: Threshold = 0.8. The majority of PSBs are accurately classified within the PSB demarcation by the model, with the misclassified lying mostly near the border.

In summary, selecting observed colors only as input features is a strategic choice that balances simplicity, efficiency, and performance. The findings presented in Figures 3, 4 and 5 demonstrate the effectiveness of ML techniques in identifying PSBs. Using observed colors derived from optical and NIR information as input features, the model without oversampling can achieve high precision (0.85) at the cost of a lower recall rate (0.1). Depending on their specific scientific goals, one can achieve higher precision but lower recall through threshold adjustment.

doi:10.6342/NTU202401965

3.4 Feature importance

Figure 6 illustrates the key features for the model with observed colors as inputs, without oversampling, in identifying PSBs. The two panels, left and right, are obtained with free random seeds, means different initial conditions in training. Due to computational limitations, the figure presents results from two single-run rather than an average of multiple runs, but it still provides valuable insight into feature importance. The top five features of the two panels in Figure 6 indicate that the combination of optical + NIR measurements is crucial for ML. The consistently most important features among the top five are $H - K_s$, $g-r$, and $g-i$, covering the entire range of optical-NIR wavelengths. Followed my study, ML cannot differentiate PSBs based only on optical or NIR measurements. Both optical and NIR measurements are necessary for an accurate classification. This means that the model for identifying PSBs requires a combination of both types of photometry. For future surveys, galaxies observed by both Rubin LSST and Euclid EWS in their overlap area are ideal for applying and further testing the model.

3.5 Redshift dependence

In this section, I investigate the model's performance across different redshift ranges. It is crucial to evaluate its applicability from this perspective. The study of precision and recall scores, determined using likelihood threshold of 0.6 and 0.8, as functions of redshift, as shown in Figure 7, reveals a clear redshift dependence in the model. Specifically, the model performs better at identifying PSBs at $z < 1$ compared to $z \gtrsim 1$, indicating most PSBs classified by the model are at $z \lesssim 1$. To understand the cause, I looked into the data distribution in the learning sample. Figure 8 clearly shows a significant drop in the

doi:10.6342/NTU202401965

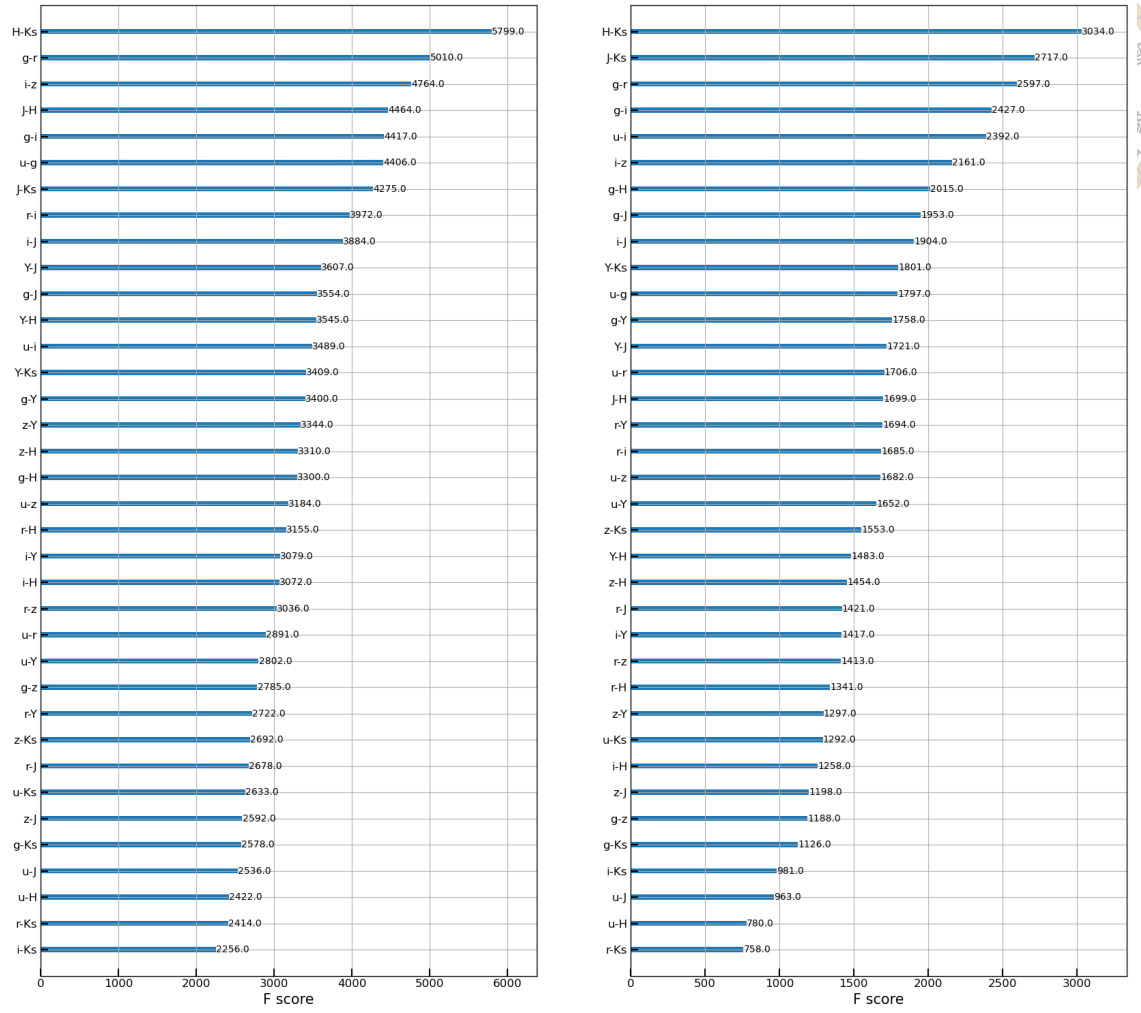

Figure 6. Two single-run results of feature importance of the model with observed colors as inputs without oversampling to identify PSBs. The top five features show that the combination of optical and NIR measurements is essential for the model to accurately identify PSBs, as neither optical nor NIR measurements alone can distinguish PSBs well.

number of both total galaxies and PSBs at redshift $z \gtrsim 1$. The redshift dependence may be primarily attributed to the lack of high-z data in the dataset. This imbalance in the training data hinders the model's ability to generalize well to PSBs at higher redshifts. The lack of PSB galaxies at higher redshifts means the model has limited examples to learn from, resulting in a preference towards recognizing PSBs at lower redshifts, where the data are more abundant.

To address the issue of redshift dependence, it is essential to incorporate more high-z PSB data into the training set. Although oversampling techniques might address the

doi:10.6342/NTU202401965

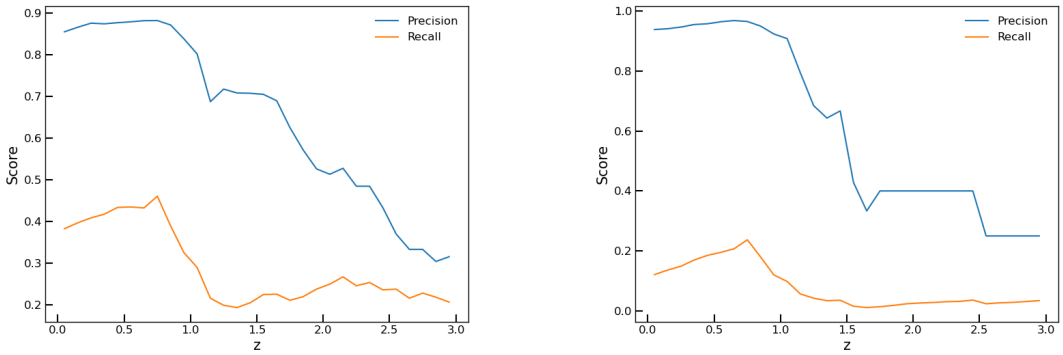

Figure 7. The precision and recall scores as functions of redshift. Scores are calculated in redshift ranging from 0.1 to 3.0 with a bin size of 0.1. Left: the model threshold is set to 0.6. Right: threshold is set to 0.8. The results indicate that the model is redshift-dependent, as it is better at identifying PSBs at $z < 1$ than at $z > 1$.

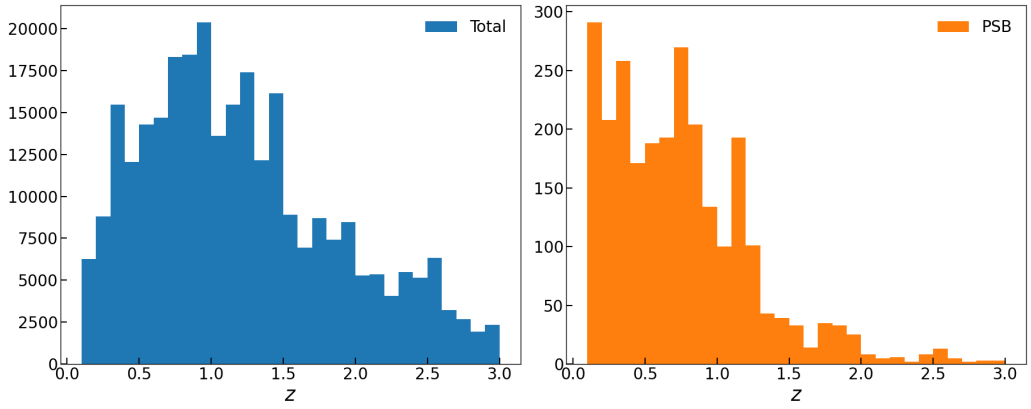

Figure 8. The number distribution of total and PSBs as a function of redshift in the learning sample. In the learning sample, there is a lack of higher-z samples as well as PSB samples at $z \gtrsim 1$.

issue, they could also lead to an increase in false positive samples (see Section 3.3). An alternative approach could involve using simulation data, which can generate true PSB samples with accurate labels.

3.6 Discussion and Model application

In this study, I introduce a new method for identifying PSBs through ML. By applying the XGBoost classifier and using observed colors derived from optical and NIR data as input, I can achieve a highly precise but less complete model. The model exhibits a strong redshift dependence, likely caused by the imbalance in the number of data points between

doi:10.6342/NTU202401965

$z < 1$ and $z \gtrsim 1$. This dependence suggests that the model is more effective at identifying PSBs at lower redshifts.

French & Zabludoff (2018), who also employed ML techniques for a similar purpose, used a random forest classifier with observed colors as input features. Their input colors were derived from photometry that spans the $ugriz$ bands, as well as NUV and IR wavelengths. They trained the model with different subsets of data at different redshifts, achieving precision scores between 60-70% and recall scores of 5-10% for PSBs at $z \sim 0.1$. Compared to their study, the model can offer prediction with much higher precision while very low recall if we apply a higher PSB threshold cut. Furthermore, as discussed in Section 3.5, the model can effectively analyze PSBs up to $z \sim 1$, indicating its capability for higher-redshift studies compared to French & Zabludoff (2018).

Both French & Zabludoff (2018) and my study suggests that there are still unknown factors affecting the ML method to identify PSBs. These factors, such as missing more photometric information, may contribute to the low recall rates, an aspect not thoroughly examined in either French & Zabludoff (2018) or my study. For future ML studies on PSBs using photometry, the features critical to accurately identifying PSBs still need to be thoroughly explored.

For the application of the model, the effectiveness in identifying PSBs relies on optical and NIR information. The upcoming Euclid EWS and Rubin LSST data will be ideal for applying this model due to their extensive wavelength coverage in the optical range by Rubin LSST and in the NIR range by Euclid EWS, over their overlapping area of $\gtrsim 8,000$ deg^2 (Euclid Collaboration et al. 2022b). Considering observed magnitudes relative to filter limits of Euclid EWS $[m_I, m_Y, m_J, m_H]$ = [26.2, 24.3, 24.5, 24.4] (Euclid

doi:10.6342/NTU202401965

Collaboration et al. 2022a) and Rubin LSST $[m_u, m_g, m_r, m_i, m_z, m_y]$ = [25.6, 26.9, 26.9, 26.4, 25.6, 24.8] (Ivezić et al. 2019) within a 1.27deg^2 area in COSMOS2020, there are 91562 galaxies with $S/N \gtrsim 5$, and 295 of them are PSBs.

Extending the number of PSBs in the COSMOS2020 to the Euclid EWS/Rubin LSST overlap area, the rough estimate suggests that there will be 500 million galaxies containing all optical and IR information detected by both Euclid EWS and Rubin LSST, and the model can label over 184,000 true PSBs with 85% precision and a 9.9% recall rate out of 1,860,000 true PSBs in the sky. If we only consider the redshift range at $z < 1$, the model can still label 131,584 PSBs out of 1,329,133 PSBs in the sky with the same precision and recall. This will be the first time that such a large number of PSBs will be studied. Until now, current research on PSBs has been limited to samples of only hundreds or a few thousand. With the forthcoming surveys that will cover nearly half of the sky and generate tens of millions of data points, traditional SED fitting will require substantial time and effort to identify PSBs. However, by applying the model to future datasets such as Euclid EWS and Rubin LSST, it will be possible to efficiently identify hundreds of thousands of true PSBs in just a few hours, significantly expanding our understanding of these galaxies.

In conclusion, the model can apply to $z \lesssim 1$ PSB studies. While it demonstrates high precision in identifying PSBs, the low recall indicates a need for further refinement. Future work should focus on incorporating more comprehensive photometric data and exploring additional features to improve the model. The upcoming Euclid EWS and Rubin LSST data offer promising opportunities for applying this model, given their extensive optical-NIR coverage over a large sky area. These datasets will create a larger sample of PSBs than ever before, allowing scientists to explore the properties and origins of PSBs, ultimately

doi:10.6342/NTU202401965

uncovering the mechanisms behind galaxy bimodality and evolution.

doi:10.6342/NTU202401965

Chapter 4 Galaxy Mass Function

The results of the number density and mass function of galaxies in the IR-selected sample are presented in this section. The definition of star-forming, quiescent, and PSB is based on the criteria described in Section 2.3. All the results are above their mass limits to ensure their robustness. All the results and discussion will focus on PSBs and their contribution to the evolution of the quiescent population.

4.1 Number density of star-forming, quiescent, and post-starburst galaxies

In Figure 9, I present the observed number density of total, star-forming, quiescent, and PSBs as a function of redshift, with masses above their mass limits. Uncertainties are calculated by combining Poisson noise, cosmic variance, and stellar mass uncertainty. Cosmic variance follows the recipe of Moster et al. (2011). I computed the stellar mass uncertainties by considering the average difference in the number of galaxies whose upper and lower limits of 68% confidence level fall within a given mass bin. Here, it can be seen that the number density of star-forming galaxies remains nearly unchanged with a slight increase, similar to the trend observed in the total population, and the number density of quiescent galaxies increases steadily toward the present day, a well-documented

doi:10.6342/NTU202401965

phenomenon in the literature (e.g., Davidzon et al. 2017; Ilbert et al. 2013; Muzzin et al. 2013; Weaver et al. 2023b). This increase in quiescent galaxies suggests a galaxy transition from blue to red. In contrast, the number density of PSBs is one to two orders of magnitude lower than that of quiescent galaxies, and the number of PSBs remains nearly unchanged at $1.0 < z < 3.0$ then begins to decline toward the present time.

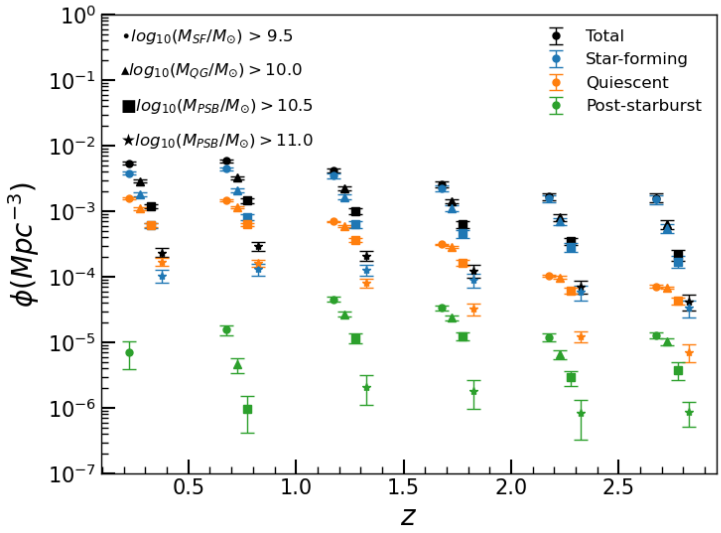

Figure 9. The observed number density of all (black), star-forming (blue), quiescent (orange), and PSB (green) galaxies as a function of redshift and mass. The mass limits are given in the top left of the figure. Uncertainties include contributions from Poisson noises, cosmic variance, and stellar mass uncertainties. For clarity, each point at the same redshift z with a different mass limit is separated with $z \pm 0.125$ or $z \pm 0.25$. The number density of PSBs at $z < 1$ declines as redshift decreases.

Figure 10 illustrates the evolution of star-forming, quiescent, and PSBs, in number density at a fixed mass and redshift, above their relative mass limits. Again, uncertainties include contributions from Poisson noise, cosmic variance, and stellar mass uncertainties. In the left-hand panel, the number densities of star-forming galaxies give us the same result as Figure 9: their number density remains nearly unchanged. In the middle panel, the number densities of quiescent galaxies grow with similar slopes, except for those with masses $log(M/M_\odot) < 10$, where the growth of low-mass quiescent galaxies occurred rapidly at $0.5 < z < 2.0$. In the right-hand panel, the number of galaxies in the PSB

doi:10.6342/NTU202401965

phase is nearly unchanged at $z > 1$. At $z < 1$ the high-mass ($log(M/M_{\odot}) > 10$) PSB systems started to decline, as indicated in Figure 9. Meanwhile, low-mass PSB systems (log(M/$M_{\odot}$) < 10) become the dominant PSB population.

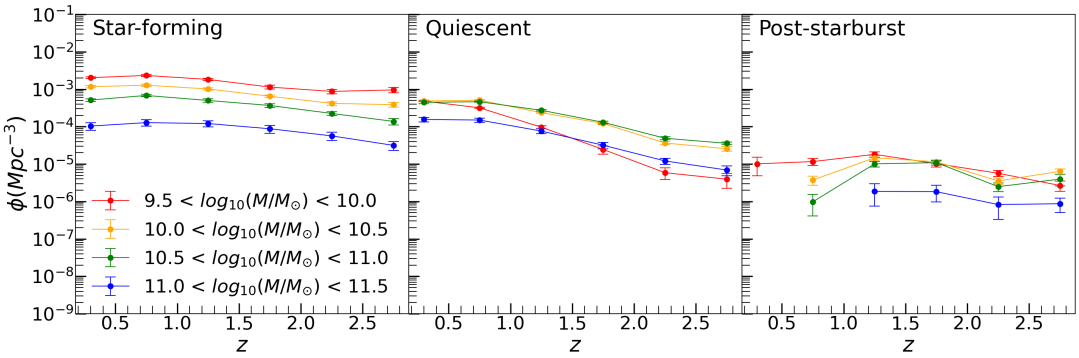

Figure 10. The evolution of number density of star-forming, quiescent, and PSBs, from left to right panels, as a function of redshift and mass. Masses are above their mass limits to ensure robustness. Uncertainties include contributions from Poisson noises, cosmic variance, and stellar mass uncertainties.

The results of Figure 9 and 10 show that the population of PSBs dominates by low-mass systems ($log(M/M_{\odot}) < 10$) at low redshifts ($z < 1$). To see the further evolution of PSBs across different masses, I present the mass functions in the next section.

4.2 Mass function of star-forming, quiescent, and post-starburst galaxies

Galaxy luminosity and mass functions can be described empirically by the parametric formulation, called Schechter function, introduced by Schechter & Press (1976). The Schechter function expressing the number density of galaxies per logarithmic mass bin $d\log M$ is defined as

$$\Phi(d\log M) = \ln(10)\Phi^* e^{-10^{\log M - \log M^*}} \times (10^{\log M - \log M^*})^{\alpha+1} d\log M \qquad (16)$$

doi:10.6342/NTU202401965

where Φ is the number density of objects per unit volume and mass, Φ^* is a normalization factor setting the overall number density of objects, M^* is a characteristic mass, and α is the low-mass-end slope of the mass function.

Numerous studies have provided evidence that the galaxy population at low redshift is more accurately described as a combination of two Schechter functions (Pozzetti et al. 2010). Each function contributes individual normalization (Φ_1^* and Φ_2^*)for low-mass and high-mass ends, as well as low-mass slopes (α_1 and α_2) while retaining a single characteristic stellar mass M^*. This so-called Double Schechter function is described as follows:

$$\Phi(d\log M) = \ln(10)e^{-10^{\log M - \log M^*}} \times [\Phi_1^*(10^{\log M - \log M^*})^{\alpha_1+1} + \Phi_1^*(10^{\log M - \log M^*})^{\alpha_1+1}] d\log M \tag{17}$$

The use of a double Schechter function is appropriate for describing the local Universe and up to $z \sim 2$, but beyond that, a single Schechter function is more suitable (Weaver et al. 2023b).

Figure 11 presents the observed mass functions at $z = 0.1 - 3.0$. The top six panels show mass functions of the star-forming, quiescent, and PSB populations in different redshift bins, while the bottom three panels compare those in each type. Uncertainties include Poisson noises, cosmic variance, and stellar mass uncertainties. The best-fit parameters derived from the single/double Schechter function are summarized in Table 2. The observed mass functions are consistent with previous studies for star-forming and quiescent galaxies (Davidzon et al. 2017; Ilbert et al. 2013; Muzzin et al. 2013; Weaver et al. 2023b). The mass functions of star-forming galaxies remain relatively similar across all redshifts. On the other hand, the mass functions of quiescent galaxies increase over time, especially for low-mass galaxies with $log(M/M_\odot) < 10$, showing a flattening at the low-mass end

doi:10.6342/NTU202401965

Table 2. Best-fit Parameters of the Single/Double Schechter Functions

Redshift	$\log(M^*/M_\odot)$	$\phi_1^*(10^{-6}\mathrm{Mpc}^{-3})$	α_1	$\phi_2^*(10^{-6}\mathrm{Mpc}^{-3})$	α_2
Star-forming					
$0.1 < z < 0.5$	10.77 ± 0.06	154.99 ± 26.96	-1.46 ± 0.02	163.75 ± 23.46	-0.31 ± 0.28
$0.5 < z < 1.0$	10.85 ± 0.07	185.26 ± 55.17	-1.40 ± 0.05	118.67 ± 30.95	-0.47 ± 0.53
$1.0 < z < 1.5$	11.00 ± 0.12	116.12 ± 42.76	-1.43 ± 0.05	47.79 ± 23.23	-0.55 ± 0.89
$1.5 < z < 2.0$	10.97 ± 0.24	76.20 ± 89.73	-1.42 ± 0.20	54.53 ± 42.93	-0.58 ± 1.73
$2.0 < z < 2.5$	10.93 ± 0.06	21.52 ± 18.21	-1.73 ± 0.17	67.01 ± 10.88	-0.77 ± 0.37
$2.5 < z < 3.0$	11.00 ± 0.14	30.70 ± 11.29	-1.67 ± 0.05	9.69 ± 5.40	0.02 ± 0.52
Quiescent					
Redshift	$\log(M^*/M_\odot)$	$\phi_1^*(10^{-6}\mathrm{Mpc}^{-3})$	α_1	$\phi_2^*(10^{-6}\mathrm{Mpc}^{-3})$	α_2
$0.1 < z < 0.5$	10.80 ± 0.04	251.03 ± 14.63	-0.29 ± 0.15	28.40 ± 10.94	-1.36 ± 0.07
$0.5 < z < 1.0$	10.90 ± 0.04	240.15 ± 26.43	-0.57 ± 0.13	0.73 ± 4.42	-1.72 ± 1.12
$1.0 < z < 1.5$	10.81 ± 0.04	155.80 ± 19.14	-0.25 ± 0.11	$0.00(3) \pm 0.04$	-2.58 ± 1.95
$1.5 < z < 2.0$	10.57 ± 0.38	88.40 ± 282.29	0.34 ± 0.56		
$2.0 < z < 2.5$	10.53 ± 0.26	29.22 ± 716.45	0.60 ± 5.06		
$2.5 < z < 3.0$	10.53 ± 0.26	29.22 ± 7.164	0.60 ± 0.51		
Post-starburst					
Redshift	$\log(M^*/M_\odot)$	$\phi_1^*(10^{-6}\mathrm{Mpc}^{-3})$	α_1	$\phi_2^*(10^{-6}\mathrm{Mpc}^{-3})$	α_2
$^*0.1 < z < 0.5$	9.16	16.90	-2.00	5.55	1.00
$0.5 < z < 1.0$	10.00 ± 0.77	3.11 ± 9.37	-2.00 ± 0.48	1.09 ± 1.71	1.00 ± 3.08
$1.0 < z < 1.5$	10.48 ± 0.14	8.29 ± 1.18	0.24 ± 0.57	0.87 ± 0.78	-1.88 ± 0.21
$1.5 < z < 2.0$	10.59 ± 0.07	7.35 ± 0.35	-0.07 ± 0.25	0.37 ± 0.34	-1.71 ± 0.24
$2.0 < z < 2.5$	10.46 ± 1.79	1.21 ± 2.73	-1.02 ± 0.73	1.05 ± 2.04	1.00 ± 4.73
$2.5 < z < 3.0$	10.42 ± 0.31	4.00 ± 5.69	0.09 ± 0.02		

Note: Some fittings will reduce to single Schechter Functions.
*Due to the lack of constraints in high-mass PSBs, the uncertainties will become unbounded.

of the quiescent galaxy mass functions at $z < 1$. The mass functions of PSBs monotonically increase as the mass decreases at $z < 1$, similar to the trends observed at the low-mass ends of the star-forming galaxy mass functions. The lower number densities of high-mass PSBs indicate that the PSB population is dominated by low-mass systems during this epoch, as discussed in Section 4.1. At $z > 1$, high-mass ($\log(M/M_\odot) > 10$) PSBs begin to emerge, and the mass functions of PSBs begin to exhibit a distinct mass peak at $log(M/M_\odot) \approx 10.5$, as shown in Table 2. The normalized mass functions of PSBs with masses $log(M/M_\odot) \gtrsim 10$, presented in Figure 12, resemble those of quiescent galaxies. These findings of the mass functions of PSBs are consistent with Wild et al. (2016) and Ichikawa & Matsuoka (2017).

In brief, the differing behaviors of the mass functions for PSBs at $z < 1$ and $z \gtrsim 1$ may indicate different contributions to the evolution of quiescent galaxies.

doi:10.6342/NTU202401965

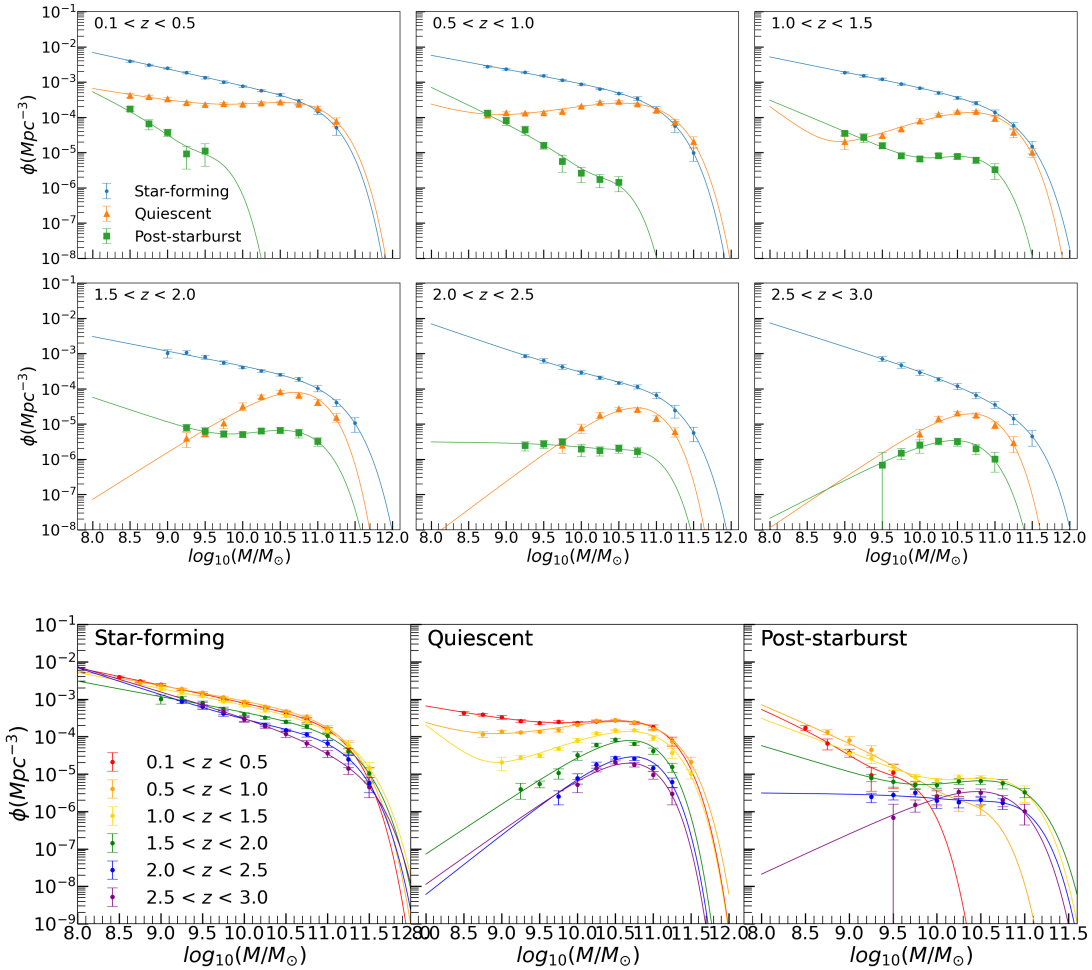

Figure 11. Top six: The mass functions of star-forming (blue), quiescent (orange), and PSB (green) galaxies in redshift bins. At $z < 1$, the mass function of PSBs increases monotonically, similar to those of low-mass star-forming galaxies. At $z > 1$, the population of low-mass PSBs ($log(M/M_{\odot}) < 10$) starts to decline, while high-mass PSBs ($log(M/M_{\odot}) > 10$) PSBs begin to emerge and dominate. Bottom three: the mass functions of the star-forming galaxies (left), passive galaxies (middle), and RQGs (right) at different redshifts. The lines represent the best-fit single/ double Shechter functions. Uncertainties include contributions from Poisson noises, cosmic variance, and stellar mass uncertainties. Here, the evolution of low- and high-mass PSBs can be seen more clearly.

4.3 The contribution of post-starburst galaxies to quiescent galaxy mass function.

In this section, I will focus solely on the evolution of galaxies through the rapid quenching path, passing the PSB phase. The contribution of PSBs to the quiescent mass function is expected to vary across different redshifts due to distinct evolutionary mechanisms op-

doi:10.6342/NTU202401965

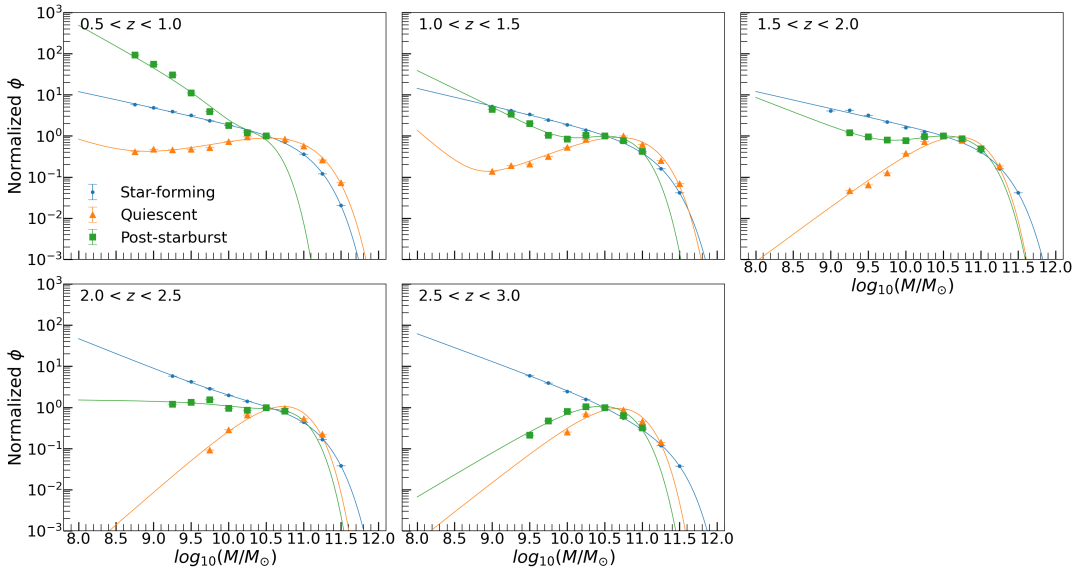

Figure 12. The normalized mass functions of star-forming, quiescent, and PSBs. The mass function has been normalized at $log(M/M_{\odot}) = 10.5$ in order to better compare their shapes. The mass function of PSBs at $\log(M/\mathrm{M}_{\odot}) > 10$ at $z > 1$ resembles that of the quiescent galaxy mass function. Note that there is a lack of PSBs with $log(M/M_{\odot}) > 10$ in the redshift bin $0.1 < z < 0.5$, so the comparison for this redshift bin is omitted.

erating during different cosmic epochs. As demonstrated and discussed in Section 4.2, the mass function of PSBs at different epochs may indicate different contributions for the high- and low-mass ends.

To examine the high- and low-mass PSB contribution to the mass function of quiescent galaxies, following the method adopted by Whitaker et al. (2012) and Wild et al. (2016), the quiescent mass functions are reproduced by adding the PSBs to the quiescent galaxies that existed in the previous redshift bin. This method is based on the assumption that all newly formed quiescent galaxies transitioned from PSBs. The reproducing formula is as follows:

$$d\phi_Q(M,z) = \frac{t_{bin}}{\tau_{PSB}} \sum_{i=1}^{N_{PSB}} \phi(M,z') \tag{18}$$

$$\phi_Q(M,z) = \phi_Q(M,z') + d\phi_Q(M,z) \tag{19}$$

doi:10.6342/NTU202401965

where z denotes the median value of a certain redshift bin, while z' denotes the median value of the previous one relative to z, $\phi_Q(M, z)$ is the mass function of quiescent galaxies at redshift z bin, $d\phi_Q(M, z)$ is the newly formed mass function of quiescent galaxies at redshift z bin, t_{bin} is the time between z bin and the previous z' bin, and τ_{PSB} is the lifetime of PSBs. The two equations, eq(18) and eq(19), describe how the quiescent galaxy mass functions are reproduced. Since quiescent galaxies cannot form new stars to grow their masses, I can reasonably assume that all quiescent galaxies in the previous z' bin will transition into the z bin. The increase in the number density of quiescent galaxies from the previous z' bin to the z bin is caused by the evolution from PSBs, as illustrated by eq(18). Therefore, the reproduced quiescent galaxy mass function in the z bin is the sum of the quiescent galaxies from the previous time (z' bin) and the newly formed quiescent galaxies transitioned from PSBs, as illustrated by eq(19).

By fitting the reproduced mass function of quiescent galaxies to the observed one at a given redshift bin, I can further constrain the lifetime of PSBs during that period. Despite the simplification of the method, it can still provide an analytical approximation of the minimum lifetime timescale of PSBs based on the scenario: Star-forming $\rightarrow$ PSB $\rightarrow$ Quiescent. Figure 13 demonstrates the reproduced quiescent galaxy mass functions based on eq(18) and eq(19), with the PSB lifetime constraints by 100 Myr and 600 Myr, the minimum and maximum values suggested by simulation (Snyder et al. 2011; Wild et al. 2009). Empirically dividing the sample into high-mass and low-mass classes with a threshold of $\log(M/M_\odot) = 10$, the reproduced quiescent galaxy mass function curves fit well in all redshift bins for high masses ($\log(M/M_\odot) > 10$) if the PSB lifetime is around 100 Myr, as the red curves presented in Figure 13. However, there are overestimated numbers of quiescent galaxies at the low-mass ends ($\log(M/M_\odot) < 10$) for $z \lesssim 1$. This result

doi:10.6342/NTU202401965

suggests that high-mass quiescent galaxies can be accounted for by the transition of PSBs with a very short lifetime scale of approximately 100 Myr, and PSBs may play a significant role in the evolution of the quiescent population. In contrast, that short time-scale evolution shows an exceeded number of low-mass quiescent galaxies at $z < 1$. Since eq(18) moves the PSB mass functions upward in parallel, the monotonic increase towards lower masses in PSB mass functions at $z < 1$ will dominate the right-hand side of eq(19), potentially leading to higher number densities in the reproduced quiescent galaxy mass functions when assuming a short lifetime scale ~ 100 Myr for PSBs. If applying a longer lifetime, e.g. 600 Myr, as the purple curves shown in Figure 13, the exceeding number of low-mass quiescent will be moderated, but there is still an overestimated number of quiescent galaxies at $z < 0.5$.

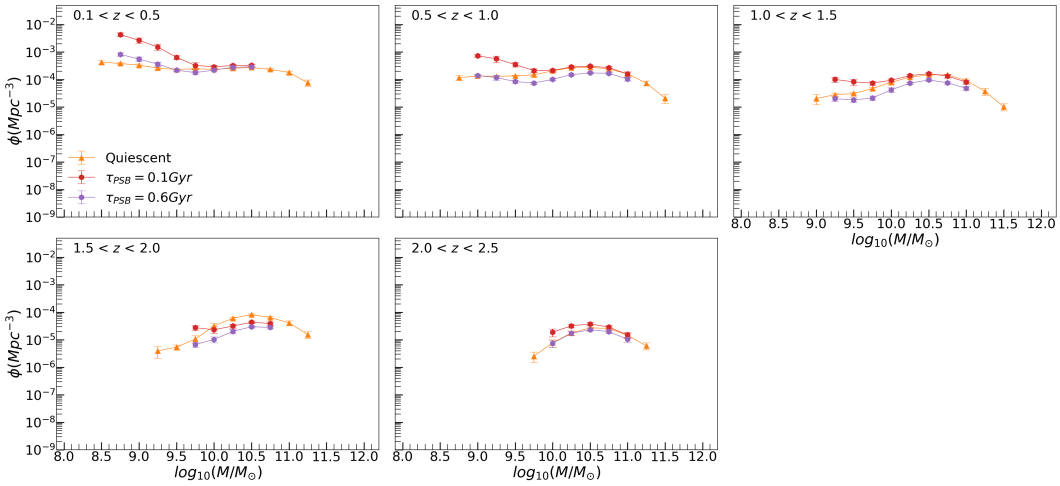

Figure 13. The reproduction of quiescent mass functions. The red and purple curves represent the reproduced mass function of quiescent galaxies plus that of PSBs with different lifetime constraints in the previous time slice, which assumes all newly formed quiescent galaxies from PSBs. The reproduced curves fit well at masses $log(M/M_{\odot}) > 10$ if the PSB lifetime is around 100 Myr, while there is an overestimated number of quiescent galaxies at the low-mass end at $z \lesssim 1$.

4.3.1 The contribution of high-mass post-starburst galaxies

The results of the PSB lifetime can be further shown in Figure 14, where the high- ($log(M/M_{\odot}) > 10$) and low-mass ($log(M/M_{\odot}) < 10$) ends of the reproduced quiescent

doi:10.6342/NTU202401965

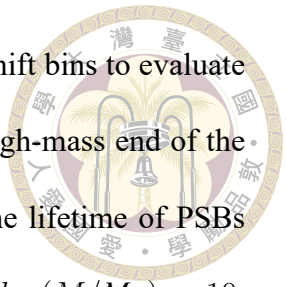

galaxy mass functions are fitted to the observed one in the same redshift bins to evaluate the best-fit PSB lifetime in each epoch. In the top five panels, the high-mass end of the mass function of quiescent galaxies fits well at all redshifts, with the lifetime of PSBs spanning around $60 - 300$ Myr. The high-mass results imply that at $log(M/M_{\odot}) > 10$, the quiescent galaxy mass functions can be largely accounted for by the transition of PSBs. These findings in high-masses PSBs are consistent with those of Wild et al. (2016) and Ichikawa & Matsuoka (2017). In contrast to the high-mass results in the top five panels of Figure 14, the low-mass fitting results of the quiescent galaxy mass functions are displayed in the bottom two panels of Figure 14. Due to the lack of quiescent galaxies and PSBs with masses $log(M/M_{\odot}) < 10$ at $z > 1$, I only show the result of low-mass fitting in the two bins: $0.1 < z < 0.5$ and $0.5 < z < 1.0$. The fittings in low-mass quiescent galaxies indicate that the flattening of the low-mass ends of the mass functions quiescent galaxies may be possibly caused by the rise of number densities in the low-mass PSBs, as suggested by literature (Wild et al. 2016; Wong et al. 2012). The fitting result for $0.5 < z < 1.0$ aligns with the suggested timescale from a few Myr to $\lesssim 1$ Gyr from both simulation (Snyder et al. 2011; Wild et al. 2009) and observation (e.g., Ciesla et al. 2016; Quintero et al. 2004). However, the longer lifetime estimate at $0.1 < z < 0.5$ introduces a conflict to the characteristic short-lived nature of PSBs. This discrepancy highlights that the assumption that all newly formed quiescent galaxies originate from PSBs cannot fully explain the mass functions of quiescent galaxies at low masses during this period.

4.3.2 The contribution of low-mass post-starburst galaxies

Because of the weirdly long best-fit lifetime of PSBs showed in the bottom two panels of Figure 14 and the exceeding number of the reproduced quiescent galaxy mass functions at low masses by introducing a shorter lifetime of PSBs presented in the first two panels

doi:10.6342/NTU202401965

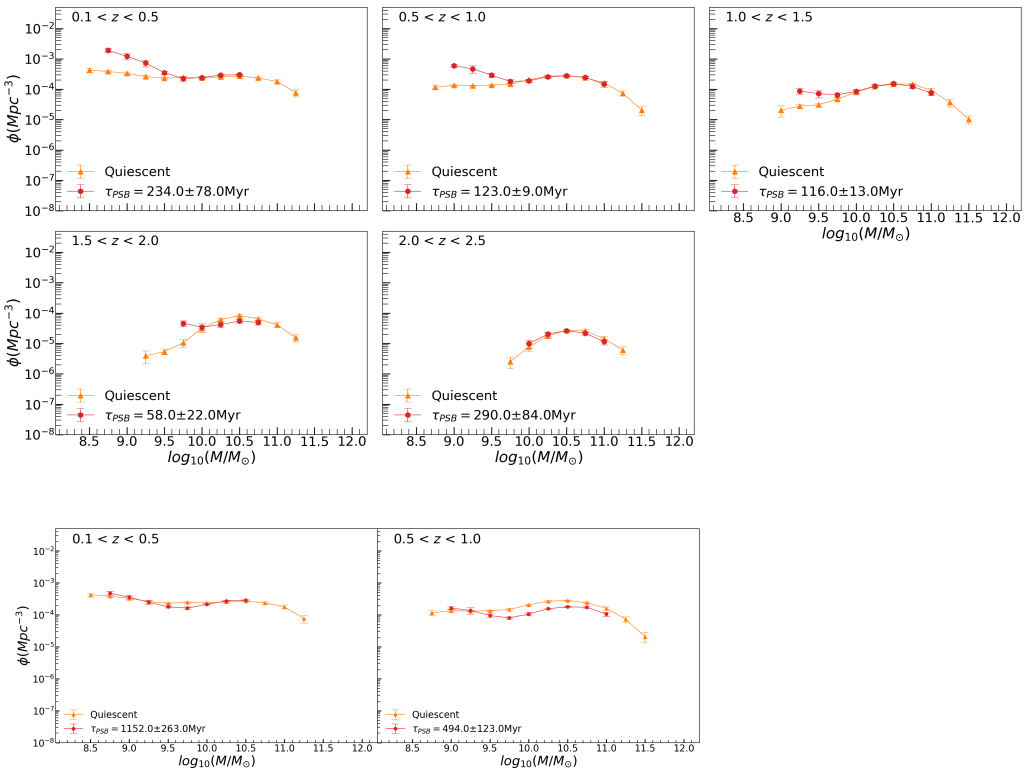

Figure 14. Top five: The reproduction of high-mass ($log(M/M_{\odot}) > 10$)quiescent galaxy mass function, based on the evolution of PSBs, and the estimated lifetimes of PSBs. The fitting performs well, with the lifetime of high-mass PSBs ranging from $\sim$ 100 to 300 Myr. Bottom two: The reproduction of low-mass ($log(M/M_{\odot}) < 10$)quiescent galaxy mass function and the estimated lifetimes of PSBs. The overestimation of the PSBs' lifetime, especially at $0.1 < z < 0.5$, indicates the necessity for more advanced assumptions.

of Figure 13 and 14, I make an assumption that some PSBs may not transition into quiescence. Dressler et al. (2013) and Arnouts et al. (2013) propose an alternative pathway for star-forming galaxies transitioning to quiescence through the PSB phase. Instead of the traditional path, they suggest a recycling scenario for PSBs: PSB $\rightarrow$ Star-forming $\rightarrow$ PSB $\rightarrow$ Quiescent. This recycling scenario suggests two stages for PSBs: they are either in the process of recycling or transitioning into quiescence. This allows me to apply a new model that introduces a new evolving pathway for PSBs at $z < 1$: quiescent galaxies will remain quiescent, and a fraction of PSBs will transition to quiescent, while others will

doi:10.6342/NTU202401965

Table 3. The Fraction f_{PSB} (%) of PSBs Transitioning into Quiescent Type in Low-mass end

	τ_{PSB} (Myr)					
Redshift	100	200	300	400	500	600
$0.1 < z < 0.5$	9 ± 1	17 ± 1	26 ± 2	34 ± 2	43 ± 3	51 ± 3
$0.5 < z < 1.0$	19 ± 3	38 ± 5	57 ± 8	76 ± 11	95 ± 13	100

return to star-forming phase.

$$d\phi_Q(M,z) = f_{PSB} \times \frac{t_{bin}}{\tau_{PSB}} \sum_{i=1}^{N_{PSB}} \phi(M,z) \tag{20}$$

By introducing an additional term f_{PSB}, which represents the fraction of the number density of PSBs that will transition into quiescence, to eq(19), this assumption, along with the relatively short lifetimes of PSBs, could resolve the "quiescent galaxy overproduction" issue at $z < 1$. Notably, there are two free parameters in this assumption, f_{PSB} and τ_{PSB}. To better understand how these two factors contribute to the formation of low-mass quiescent galaxies, I set the lifetime value within the suggested range by Wild et al. (2009) and derive the potential fraction of PSBs that transition into quiescence. The results are summarized and presented in Table 3. Based on the best-fit PSB lifetime scales derived from the high-mass results, which range from 60 to 300 Myr, the fraction of PSBs transitioning into quiescence (f_{PSB}) would be approximately 10% to 30% at $0.1 < z < 0.5$ and around 20% to 60% at $0.5 < z < 1.0$. Under the new model, some PSBs will transition to quiescence and remain in that state, while others return to star-forming. Despite the simplicity and effectiveness of the new assumption in accounting for the contribution of PSBs to the build-up of low-mass quiescent galaxy mass functions at $z < 1$, it remains theoretical and requires further validation through additional testing.

In conclusion, I examined the contribution of PSBs to the quiescent mass function at both high and low masses by fitting the reproduced mass function to the observed one

doi:10.6342/NTU202401965

within a given redshift bin. The buildup of the quiescent mass functions at high and low masses can be attributed to the transition of PSBs. Based on high-mass results, PSBs exhibit lifetimes ranging from 60 to 300 Myr. To explain the mass functions of quiescent galaxies at $z < 1$, a new assumption is introduced: only part of PSBs would transition to quiescence. If the lifetime of PSBs is the same scale of the high-mass results, less than 60% of PSBs would become quiescent galaxies. Despite the success of the new assumption in accounting for the mass functions of quiescent galaxies at low masses, further testing is still required.

4.4 Discussion

In Section 4.3, I reproduced the mass functions of quiescent galaxies from the PSB mass functions across five redshift bins using two analytical models. The high-mass results align with the findings of previous studies (Ichikawa & Matsuoka 2017; Wild et al. 2016). For the low-mass end, the recycling model of PSBs successfully accounts for the buildup of the quiescent galaxy mass functions, suggesting that not all PSBs will transition to quiescent galaxies. This finding implies that the recycling of galaxies may play a significant role in the broader picture of galaxy evolution, highlighting the need for further investigation into the transitional processes of these galaxies.

In addition, despite the successes of these two analytical models, there are still some incompleteness/caveat of them.

1. If some galaxies transform from star-forming to quiescent with a long time (slow path), they do not become PSBs at all. Considering their presence in both models,

doi:10.6342/NTU202401965

the estimated lifetime of PSBs will become longer, as described in eq(21).

$$d\phi_Q(M,z) = f_{PSB} \times \frac{t_{bin}}{\tau_{PSB}} \sum_{i=1}^{N_{PSB}} \phi(M,z) + d\phi_{slow}(M,z) \tag{21}$$

The introduction of galaxies following the slow path ($d\phi_{slow}(M,z)$) diminishes the contribution from PSBs, meaning the contribution from the factor $f_{PSB} \times \frac{t_{bin}}{\tau_{PSB}}$ will lessen. For the high-mass PSBs, f_{PSB} is 1, this model will result in a longer PSB lifetime τ_{PSB} than discussed in Section 4.3.1. For low-mass PSBs and considering a shorter lifetime for them at $z < 1$, this model will suggest a lower fraction of PSBs transitioning into quiescence than discussed in Section 4.3.2.

2. If some quiescent galaxies can revert to being star-forming, the contribution can be modeled as follows.

$$d\phi_Q(M,z) = f_{PSB} \times \frac{t_{bin}}{\tau_{PSB}} \sum_{i=1}^{N_{PSB}} \phi(M,z) - d\phi_{Q\to SF}(M,z) \tag{22}$$

Due to the additional negative term from $d\phi_{Q\to SF}(M,z)$, the contribution from the factor $f_{PSB} \times \frac{t_{bin}}{\tau_{PSB}}$ of PSBs will be enhanced to cancel out the additional term. For high-mass PSBs, this will lead to a shorter lifetime of PSBs τ_{PSB} than discussed in Section 4.3.1. For low-mass PSBs, and considering a shorter lifetime for them at $z < 1$, the model suggests a higher fraction of PSBs transitioning into quiescence than discussed in Section 4.3.2.

doi:10.6342/NTU202401965

Chapter 5 Summary and Conclusions

I have used the COSMOS2020 catalog to build a ML classification model and explore the mass function of PSBs at redshift $0.1 < z < 3.0$ in the COSMOS field. My findings are summarized as follows.

1. ML techniques can identify PSBs. With optical and NIR information, the model can achieve high precision (0.85) while sacrificing the recall rate (0.1). Depending on their specific scientific goals, one can achieve higher precision but lower recall through threshold adjustment. This model performs better in precision and recall at $z \lesssim 1$ than at $z \gtrsim 1$, indicating its suitability for studies within this redshift range.

2. These ML results can be applied to the optical and NIR data from the extensive regions covered by the Euclid EWS and Rubin LSST surveys, as well as future all-sky surveys, enabling the efficient identification and creation of a large sample of up to 184,000 true PSBs with a precision of 0.85 and a recall of 0.1. If we only consider the redshift range at $z < 1$, the model can still label 131,584 PSBs with the same precision and recall.

3. The mass function of PSBs exhibits a monotonic increase toward the low-mass end at $z \lesssim 1$, and the population of PSBs is dominated by low masses during that period, while at $z > 1$ at $log(M/M_{\odot}) > 10$, the mass function of PSBs resembles that of

doi:10.6342/NTU202401965

quiescent galaxies.

4. High-mass PSBs with masses $log(M/M_{\odot}) > 10$ can largely explain the buildup of high-mass quiescent galaxy mass function, with their lifetimes ranging from 100 to 300 Myr.

5. Low-mass PSBs with masses $\log(M/M_{\odot}) < 10$ can also account for the flattening in low-mass quiescent galaxy mass function at $z < 1$, although with a longer PSB lifetime estimate > 1 Gyr. Assuming that some PSBs revert to star-forming galaxies can address the issue of overestimating PSB lifetimes at the low-mass end. This adjustment suggests that less than 60% of PSBs would transition into quiescent galaxies, though further testing is required to confirm this.

For evolutionary studies of galaxies, it is crucial to consider the role of recycling in the broader picture of galaxy evolution. To thoroughly test this, larger area and deeper surveys will be needed to fully quantify these processes, especially for PSBs. The ML part of this study serves as preliminary work for the forthcoming Euclid EWS/Rubin LSST data. Applying my model to these datasets will generate an unprecedentedly large sample of PSBs, potentially numbering hundreds of thousands. This extensive dataset will enable scientists to study PSBs in greater detail, ultimately enhancing our understanding of the mechanisms driving galaxy bimodality and evolution.

doi:10.6342/NTU202401965

References

Aihara, H., AlSayyad, Y., Ando, M., et al. 2019, PASJ, 71, 114

Arnouts, S., Le Floc'h, E., Chevallard, J., et al. 2013, A&A, 558, A67

Arnouts, S., Moscardini, L., Vanzella, E., et al. 2002, MNRAS, 329, 355

Belli, S., Newman, A. B., & Ellis, R. S. 2019, ApJ, 874, 17

Bertin, E. 2010, SWarp: Resampling and Co-adding FITS Images Together, Astrophysics Source Code Library, record ascl:1010.068

Bertin, E. & Arnouts, S. 1996, A&AS, 117, 393

Brammer, G. B., van Dokkum, P. G., & Coppi, P. 2008, ApJ, 686, 1503

Bruzual, G. & Charlot, S. 2003, MNRAS, 344, 1000

Chabrier, G. 2003, PASP, 115, 763

Ciesla, L., Boselli, A., Elbaz, D., et al. 2016, A&A, 585, A43

Civano, F., Marchesi, S., Comastri, A., et al. 2016, ApJ, 819, 62

Couch, W. J. & Sharples, R. M. 1987, MNRAS, 229, 423

Davidzon, I., Ilbert, O., Laigle, C., et al. 2017, A&A, 605, A70

doi:10.6342/NTU202401965

Dressler, A. & Gunn, J. E. 1983, ApJ, 270, 7

Dressler, A., Oemler, Augustus, J., Poggianti, B. M., et al. 2013, ApJ, 770, 62

Dressler, A., Smail, I., Poggianti, B. M., et al. 1999, ApJS, 122, 51

Euclid Collaboration, Moneti, A., McCracken, H. J., et al. 2022a, A&A, 658, A126

Euclid Collaboration, Scaramella, R., Amiaux, J., et al. 2022b, A&A, 662, A112

French, K. D. & Zabludoff, A. I. 2018, ApJ, 868, 99

Goto, T. 2005, MNRAS, 357, 937

Hsieh, B.-C., Wang, W.-H., Hsieh, C.-C., et al. 2012, ApJS, 203, 23

Ichikawa, A. & Matsuoka, Y. 2017, ApJL, 843, L7

Ilbert, O., Arnouts, S., McCracken, H. J., et al. 2006, A&A, 457, 841

Ilbert, O., McCracken, H. J., Le Fèvre, O., et al. 2013, A&A, 556, A55

Ivezić, Ž., Kahn, S. M., Tyson, J. A., et al. 2019, ApJ, 873, 111

Kauffmann, G., Heckman, T. M., White, S. D. M., et al. 2003, MNRAS, 341, 54

Laigle, C., McCracken, H. J., Ilbert, O., et al. 2016, ApJS, 224, 24

Lang, D., Hogg, D. W., & Mykytyn, D. 2016, The Tractor: Probabilistic astronomical source detection and measurement, Astrophysics Source Code Library, record ascl:1604.008

Marchesi, S., Civano, F., Elvis, M., et al. 2016, ApJ, 817, 34

McCracken, H. J., Milvang-Jensen, B., Dunlop, J., et al. 2012, A&A, 544, A156

doi:10.6342/NTU202401965

Milvang-Jensen, B., Freudling, W., Zabl, J., et al. 2013, A&A, 560, A94

Moneti, A., McCracken, H. J., Hudelot, W., et al. 2023, VizieR Online Data Catalog, II/373

Moster, B. P., Somerville, R. S., Newman, J. A., & Rix, H.-W. 2011, ApJ, 731, 113

Muzzin, A., Marchesini, D., Stefanon, M., et al. 2013, ApJ, 777, 18

Noirot, G., Sawicki, M., Abraham, R., et al. 2022, MNRAS, 512, 3566

Oke, J. B. & Gunn, J. E. 1983, ApJ, 266, 713

Peng, Y.-j., Lilly, S. J., Kovač, K., et al. 2010, ApJ, 721, 193

Polletta, M., Tajer, M., Maraschi, L., et al. 2007, ApJ, 663, 81

Pozzetti, L., Bolzonella, M., Zucca, E., et al. 2010, A&A, 523, A13

Quintero, A. D., Hogg, D. W., Blanton, M. R., et al. 2004, ApJ, 602, 190

Sawicki, M., Arnouts, S., Huang, J., et al. 2019, MNRAS, 489, 5202

Schechter, P. & Press, W. H. 1976, ApJ, 203, 557

Schmidt, M. 1968, ApJ, 151, 393

Snyder, G. F., Cox, T. J., Hayward, C. C., Hernquist, L., & Jonsson, P. 2011, ApJ, 741, 77

Szalay, A. S., Connolly, A. J., & Szokoly, G. P. 1999, AJ, 117, 68

Taniguchi, Y., Kajisawa, M., Kobayashi, M. A. R., et al. 2015, PASJ, 67, 104

Taniguchi, Y., Scoville, N., Murayama, T., et al. 2007, ApJS, 172, 9

doi:10.6342/NTU202401965

Weaver, J., Zalesky, L., Allen, N., & Taamoli, S. 2023a, The Farmer: Photometry routines for deep multi-wavelength galaxy surveys, Astrophysics Source Code Library, record ascl:2312.016

Weaver, J. R., Davidzon, I., Toft, S., et al. 2023b, A&A, 677, A184

Weaver, J. R., Kauffmann, O. B., Ilbert, O., et al. 2022, ApJS, 258, 11

Whitaker, K. E., Kriek, M., van Dokkum, P. G., et al. 2012, ApJ, 745, 179

Wild, V., Almaini, O., Cirasuolo, M., et al. 2014, MNRAS, 440, 1880

Wild, V., Almaini, O., Dunlop, J., et al. 2016, MNRAS, 463, 832

Wild, V., Kauffmann, G., Heckman, T., et al. 2007, MNRAS, 381, 543

Wild, V., Walcher, C. J., Johansson, P. H., et al. 2009, MNRAS, 395, 144

Williams, R. J., Quadri, R. F., Franx, M., van Dokkum, P., & Labbé, I. 2009, ApJ, 691, 1879

Wong, O. I., Schawinski, K., Kaviraj, S., et al. 2012, MNRAS, 420, 1684

Wright, E. L. 2006, PASP, 118, 1711

Wu, P.-F., van der Wel, A., Bezanson, R., et al. 2020, ApJ, 888, 77

Yang, Y., Zabludoff, A. I., Zaritsky, D., & Mihos, J. C. 2008, ApJ, 688, 945

Zabludoff, A. I., Zaritsky, D., Lin, H., et al. 1996, ApJ, 466, 104

Zamojski, M. A., Schiminovich, D., Rich, R. M., et al. 2007, ApJS, 172, 468

doi:10.6342/NTU202401965

Appendix A — The Effect of Rest-frame Color Uncertainties

In Section 2.3, the PSB criteria are defined by $NUV - r > 2.5$ and $r - J < 0.5$. However, the boundaries for defining PSBs can vary due to systematic effects, such as SED fitting, dust context, etc., resulting in uncertainties in the color classifications and further mass functions. To examine the systematic uncertainties of the definition of " PSB" galaxies affecting the mass functions of itself, as well as the lifetime I estimated in the previous sections, I vary the bounds of the PSB population within the $NUVrJ$ diagram by ± 0.1 mag in both $NUV - r$ and $r - J$. Due to the rarity of PSBs, it is expected that the mass function of PSBs would vary depending on the definition of PSB. The other two classes, star-forming and quiescent, do not differ, or remain the same, as I got in Section 4.2.

Figure 15, 16, and 17 show the impact of rest-frame color uncertainties on mass functions of star-forming, quiescent, and PSB galaxies using the maximum, minimum, and median values. The mass functions of star-forming galaxies remain unchanged, as do those of quiescent galaxies, but the mass functions of PSB galaxies vary greatly. Despite the variations, the behavior of the PSB mass function discussed in previous sections remains valid: (1) at $z < 1$, the mass function of PSBs increases monotonically, similar

doi:10.6342/NTU202401965

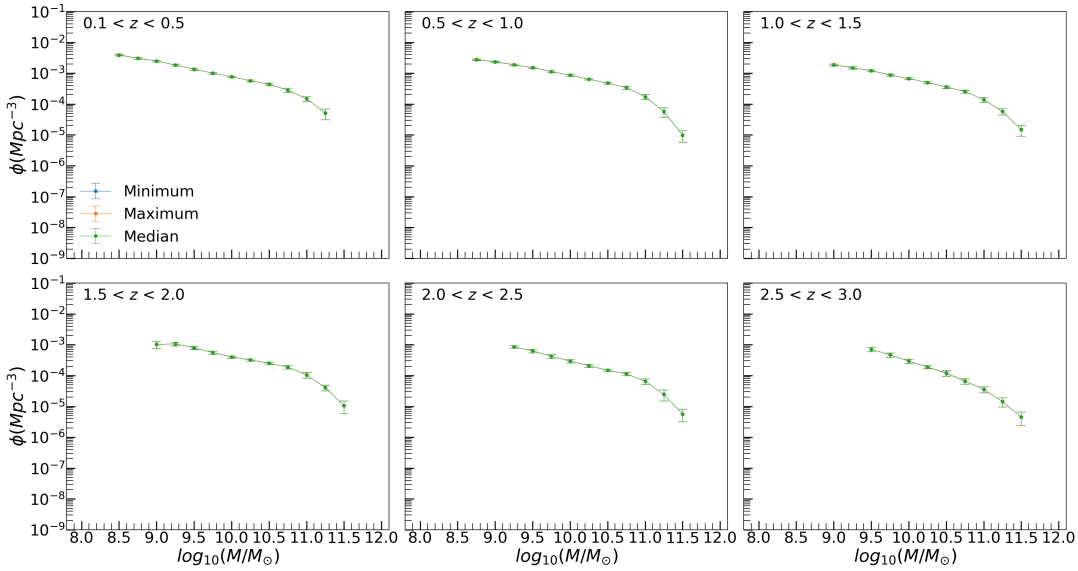

Figure 15. The impact of rest-frame color uncertainties on the mass function of star-forming galaxies in six redshift bins using minimum, maximum, and median curves. The mass functions of star-forming galaxies are unchanged.

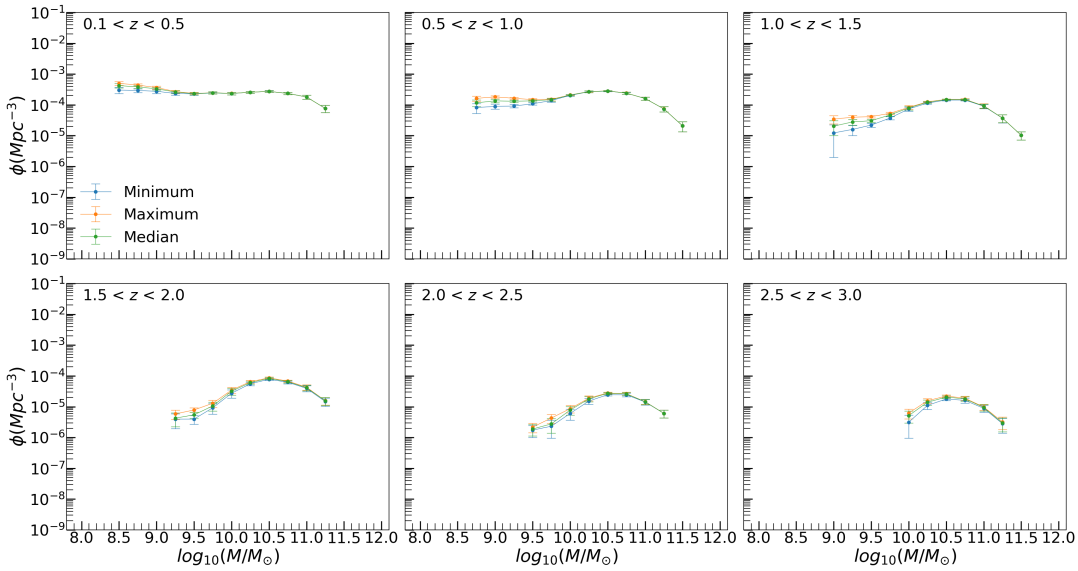

Figure 16. The impact of rest-frame color uncertainties on the mass function of quiescent galaxies in six redshift bins using minimum, maximum, and median curves. The mass functions of quiescent galaxies are nearly unchanged.

to that of star-forming galaxies at low masses; (2) at $z > 1$, the population of high-mass ($log(M/M_{\odot}) > 10$) PSBs begin to emerge and dominate; (3) at $z > 1$, the mass function begins to exhibit a distinct peak at $log(M/M_{\odot}) \approx 10.5$. These observations point to two quenching mechanisms: secular quenching and environmental quenching.

doi:10.6342/NTU202401965

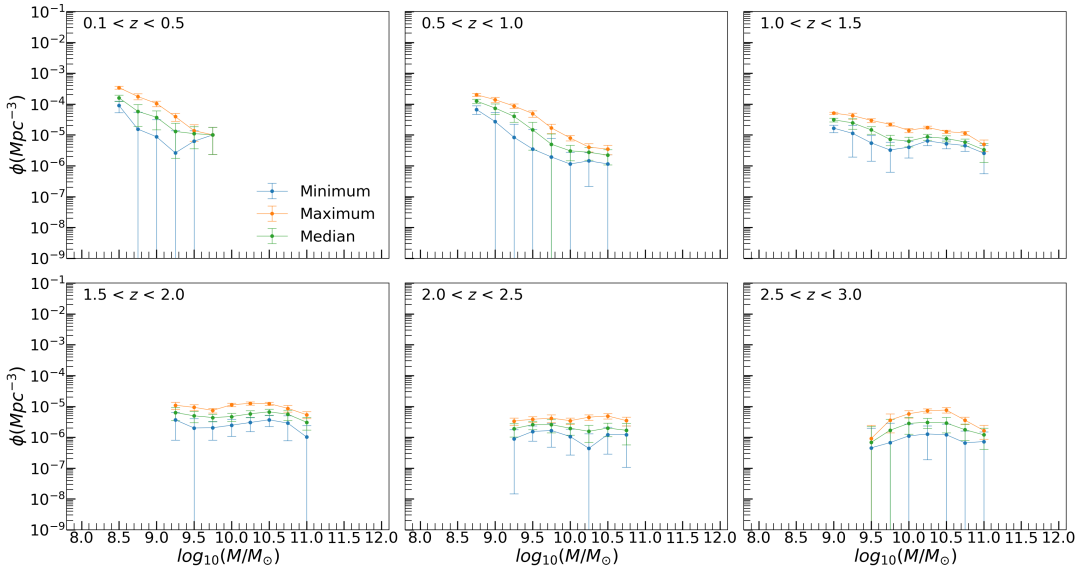

Figure 17. The impact of rest-frame color uncertainties on the mass function of PSBs in six redshift bins using minimum, maximum, and median curves. The mass functions of PSB galaxies vary greatly.

Table 4. The Impact of Rest-frame Color Uncertainties on the Lifetime of PSBs in High-mass end

	τ_{PSB} (Myr)		
Redshift	Min	Med	Max
*$0.1 < z < 0.5$	104.0 ± 28.0	277.0 ± 77	607.0 ± 160.0
$0.5 < z < 1.0$	87.0 ± 8.0	123.0 ± 9.0	266.0 ± 39.0
$1.0 < z < 1.5$	61.0 ± 8.0	116.0 ± 13.0	223.0 ± 34.0
$1.5 < z < 2.0$	34.0 ± 14.0	58.0 ± 22.0	100.0 ± 22.0
$2.0 < z < 2.5$	157.0 ± 59.0	331.0 ± 163.0	637.0 ± 210.0

* Due to a lack of high-mass PSB galaxies in some color selections at this redshift, the lifetime will become much uncertain.

Then, the lifetime of high-mass PSB galaxies ($\log(M/M_{\odot}) > 10$) is estimated for each epoch, as shown in Table 4. The table presents the minimum, median, and maximum lifetime values. The lifetime of PSBs ranges from approximately 50 to 600 Myr, falling within the suggested timescale found in the literature.

Table 5 presents the impact of rest-frame color uncertainties on the fraction of PSBs transitioning into quiescence in the low-mass end. The lower values of f_{PSB} at the redshift bin $0.1 < z < 0.5$ implies fewer PSBs would transition into quiescence.

doi:10.6342/NTU202401965

Table 5. The Impact of Rest-frame Color Uncertainties on the Fraction f_{PSB} (%) of PSBs Transitioning into Quiescence in Low-mass End

	τ_{PSB} (Myr)						
Redshift	100	200	300	400	500	600	
$0.1 < z < 0.5$	5 ± 0	10 ± 0	14 ± 0	19 ± 1	24 ± 1	29 ± 1	(Min)
	9 ± 1	17 ± 1	26 ± 2	34 ± 2	43 ± 3	51 ± 3	(Med)
	19 ± 8	39 ± 17	58 ± 25	78 ± 33	97 ± 41	100	(Max)
$0.5 < z < 1.0$	9 ± 1	18 ± 1	27 ± 2	36 ± 2	45 ± 3	55 ± 4	(Min)
	19 ± 3	38 ± 5	57 ± 8	76 ± 11	95 ± 13	100	(Med)
	39 ± 15	78 ± 29	100	100	100	100	(Max)

doi:10.6342/NTU202401965